Title
Thermal Conductivity of SmB6 Under Uniaxial Strain

Author
Yu, Agnes Laura

Publication Date
2022

UNIVERSITY OF CALIFORNIA,
IRVINE

Thermal Conductivity of SmB_6 Under Uniaxial Strain

DISSERTATION

submitted in partial satisfaction of the requirements
for the degree of

DOCTOR OF PHILOSOPHY

in Physics

by

Agnes Laura Yu

Dissertation Committee:
Professor Jing Xia, Chair
Assistant Professor Luis A. Jauregui
Assistant Professor Judit Romhanyi

2022

DEDICATION

I would like to dedicate my dissertation work to my father and my younger sister Sophia Yu, as they both have been there for me during my most difficult times.

TABLE OF CONTENTS

LIST OF FIGURES

linear term for κ/T was extrapolated via a linear fit of T^2, which yields values in the order of 10^{-1} mW K^{-2} cm^{-1} for both unstrained and strained SmB_6.

ACKNOWLEDGEMENTS

I would like to express my deepest gratitude to my academic advisor Jing Xia for granting me an opportunity to work in his lab and his invaluable guidance in experimental physics. I have learned and accomplished much more than I ever thought I could, and I will forever be grateful.

I would also like give my big thanks to my colleagues Brian Casas, Jingyuan Wang, Camron Farhang, Laisi Chen, and Alex Stern for generously helping me out so many times, as well as their utmost patience. My time here at UCI would have been infinitely more difficult without their help and I have learned so many things while working with them.

Lastly, my immense love and thanks go to my friends and family. You guys were my light during my time in graduate school. Thank you Alexandra, Tien, and Anna for your friendship. Thank you Apa for always trying to help me. And thank you Sophia for being my rock.

VITA

Agnes Laura Yu

EDUCATION

Ph.D. in Physics **2022**

University of California, Irvine

Bachelor of Science in Physics **2016**

University of California, Irvine

RESEARCH EXPERIENCE

Graduate Research Assistant **2018 – 2022**

X-Lab, University of California, Irvine

Undergraduate Research Assistant **2015 – 2016**

BioMEMS Laboratory, University of California, Irvine

Undergraduate Research Assistant **2014**

Asantha Cooray Group, University of California, Irvine

TEACHING EXPERIENCE

Graduate Teaching Assistant **2017 – 2020**

University of California, Irvine

ABSTRACT OF THE DISSERTATION

Thermal Conductivity of SmB_6 Under Uniaxial Strain

by

Agnes Laura Yu

Doctor of Philosophy in Physics

University of California, Irvine, 2022

Professor Jing Xia, Chair

SmB_6 is a mixed valent Kondo insulator with a conducting surface state and an insulating bulk at low temperatures, with this feature possibly being topological. Even though there is some idea of the nature of the surface state, the bulk of SmB_6 has been generally ambiguous. This is due to several quantum oscillation and thermal conductivity studies having contradicting observations from each other. Two quantum oscillation studies of SmB_6 have been noted to reach incompatible conclusions regarding the dimensionality of the Fermi surface. One of the studies have observed a 2D Fermi surface associated with the metallic surface while the other a 3D Fermi surface attributed with the insulating bulk. However, insulators do not have a Fermi surface, so if there was a 3D Fermi surface due to the insulating bulk, this would mean that the Fermi surface exists due to some charge neutral fermions. Thermal conductivity κ measurements allow probing of bulk states due to the measurement of the carried entropy by carriers regardless of their charge and spin. Three studies that measured the thermal conductivity of SmB_6 have also not reached a unanimous conclusion, as one of the studies measured a non-negligible residual linear κ. The possible origin as to why these measurements do not agree with each other may be due to intrinsic differences of the sample. For example, the floating-zone grown SmB_6 samples are known to have samarium deficiencies that may act as $J = 5/2$ magnetic impurities. Electrical

transport measurement of SmB_6 have demonstrated that the bulk and the surface changes dramatically with changes in pressure. Extending to this, our group have adopted a strain apparatus that uses tri-piezo technique in order to have controllable application of the mechanical strain for electrical measurements of SmB_6, which it was discovered that surface conduction exists up to 200K with 0.7% tensile strain. We have developed a symmetrized design that utilizes the same uniaxial strain apparatus for our thermal conductivity measurements in order to simulate lattice distortion effects from samarium deficiencies present in floating-zone grown crystals, applying 0.27% uniaxial tensile strain to a flux-grown SmB_6.

Chapter 1

Introduction

1.1 Overview of SmB_6

Samarium hexaboride (SmB_6) is a simple cubic compound with its unit cell containing six boron atoms arranged in an octahedral structure and one samarium atom, as shown in Figure 1.1 (a). The lattice constant, or the size of the unit cell, is a = 4.133 Å for SmB_6 [1]. Even though SmB_6 has been studied for over 50 years, the nature of its ground state is not fully resolved. In 1969, SmB_6 was discovered to transition from a paramagnetic metal at room temperature to a narrow-gapped paramagnetic insulator under low temperatures [2]. Before this discovery in 1969, magnetic materials with f-electrons were believed to be electronically inert [2]. There was no evidence for magnetic ordering down to 0.35 K, so the samarium ion was concluded to be divalent with a $4f^6$ (Sm^{2+}) configuration at low temperatures. At higher temperatures, a Curie-Weiss-like susceptibility behavior was observed, which was attributed to a transitioned trivalent $4f^5$ (Sm^{3+}) state [3]. However, in 1970, a new analysis for the electronic configuration of SmB_6 was presented, showing that the susceptibility measurements fitted well with a presence of 40% divalent and 60% trivalent samarium ions [4]. Around the same time, pressurized SmS was discovered to exhibit similar behavior as SmB_6 [5], leading to the discovery of the non-integer valence of the samarium ion caused by the fluctuations between the $4f^6$ and the $4f^5$ state, which averages out to $Sm^{2.6+}$.

What was understood so far was that the 4f ionization energy levels were separated by a large Coulomb interaction, where at least one of the bands crosses the band of conduction electrons. The width of the 4f band broadens, with the Fermi energy located at the broadened peak [6,7]. However, by this explanation alone, SmB_6 would be considered only a metal. A gap between the energy bands has to exist at the Fermi energy in order for SmB_6 to be an insulator. Further studies have led to the explanation that the gap exists by the localized f-electrons hybridizing with the delocalized d-electrons, opening up a hybridization energy gap [8–11]. This can be modeled by a Kondo lattice, or a lattice of localized moments immersed in the sea of conduction electrons. The model is related to the Kondo effect, which describes the scattering of the conduction electrons by the magnetic moment, and this scattering is enhanced under low temperatures [12]. For certain exchange interaction strength between the f and the d electrons relative to the bandwidth of the conduction band, a hybridization gap, also known as the Kondo gap, forms between the d- and the f-bands at $\Delta \sim$ 40K [10,11]. The utilization of the Kondo lattice model to explain the insulating behavior is the reason why SmB_6 is referred to as a Kondo insulator.

The low-temperature insulating state of SmB_6 was verified in 1979 when the Hall coefficient $R_H = 1/ne$ (n being the carrier density) was measured, where it was discovered that the resistivity at T→0 K was 10^4 larger than the resistivity at room temperature. This increase was too significant to be caused by the scattering of metallic carriers, and so was attributed to carrier decrease, which is consistent with the carrier density of an insulator being temperature-dependent [13].

Even though the resistivity plateau at 4K [Figure 1.1(b)] was observed much earlier, the possible mechanism for its emergence was unclear (as previously proposed explanations were found to be unphysical [13,14]) until 2010 when SmB_6 was theoretically proposed to be a topological insulator [2]. The main feature of the topological insulator is the non-trivial topologically protected metallic surface with an insulating bulk. This topological surface state could become insulating by breaking time-reversal symmetry, which is done by doping with magnetic impurities like gadolinium, or could be weakened with an application of a small magnetic field [2, 19]. Various other studies have supported SmB_6 being a topological insulator, such as ARPES experiments [15–17], thickness independent transport [18,19], spin-polarized transport [20], and STM [21–23], though there have been other studies that have challenged this notion.

Although there may be a general acceptance of the surface state being topological in nature, the insulating bulk state is quite ambiguous. Two studies have focused on quantum oscillation measurements using torque magnetometry via the de Haas-van Alphen (dHvA) effect, which allows the probing of the Fermi surface topology and the changes to it caused by Landau level quantization. Both studies have reached contradictory conclusions regarding the Fermi surface of SmB_6 [24,25]. The study conducted by Li et al. used the flux-grown SmB_6 sample provided by our group and observed a 2D Fermi surface, which was attributed to the metallic surface state [24]. However, this would contradict the well-known behavior of SmB_6 as a small gap bulk insulator [15,26,27]. Another study was conducted by Tan et al. that observed quantum oscillations that were characteristic of a 3D Fermi surface and were associated with an “unusual” insulating bulk state and having the characteristics of some “unconventional” Fermi liquid, as insulators would not have a Fermi surface [25]. This “unconventional” characteristic also included their quantum oscillations not having a Lifshitz-Kosevich temperature dependence that is typically observed in many of the strongly correlated electron systems.

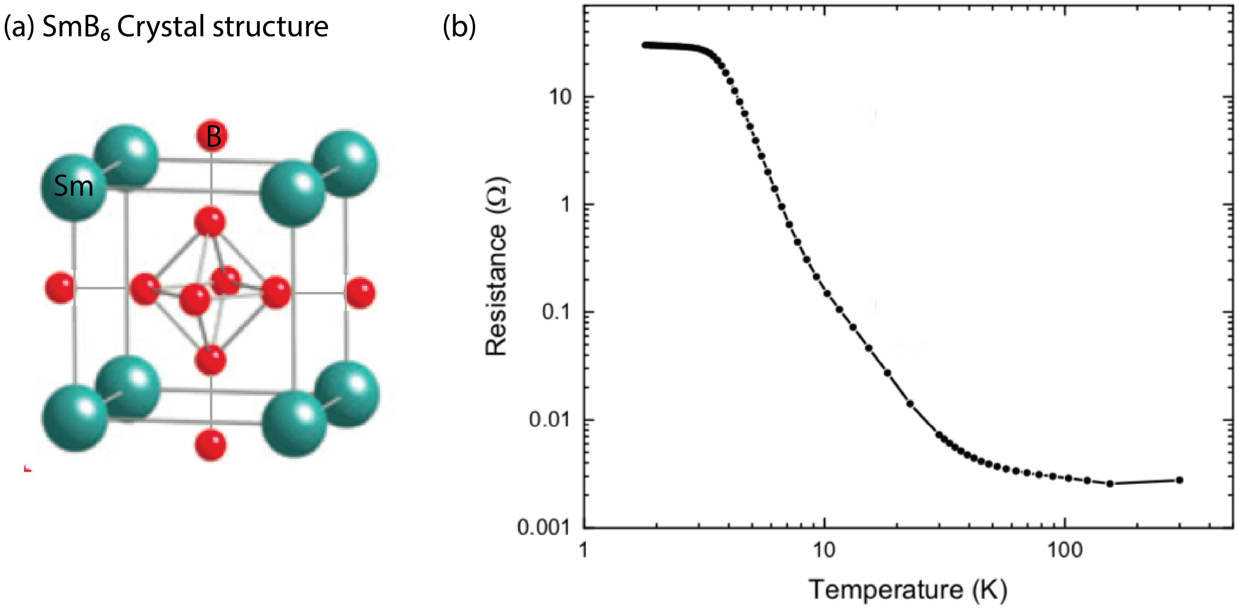

Figure 1.1. (a) Crystal structure of SmB_6. (b) Resistance versus temperature of a single flux grown SmB_6. A Kondo gap opens ~40K as shown by the thermally activated behavior, with the resistance saturation occuring at ~4K.

Another method of detecting possible charge-neutral fermionic excitations would be by measuring the thermal conductivity κ of the sample. Thermal transport measurements allow the bulk excitations to be probed since the entropy of the system is being measured and has the added advantage of differentiating the contribution made by each energy carrier (bosons and fermions). The differentiation is done by using the known temperature dependence of each carrier to extrapolate their contribution. Since the surface state is metallic for SmB_6 under low temperatures, it was found that electrons contributed to some negligible κ. So far, three studies have focused on the thermal conductivity of SmB_6 [28–30], with one study [30] finding a non-negligible residual linear term of κ that indicates some charge-neutral fermionic contribution. Thermodynamic evidence was presented for this case, where for fermionic excitations at sufficiently high enough temperatures, the electronic contribution can be eliminated as the cause. However, this has not been experimentally confirmed [30].

In order to explain the observation of quantum oscillations and the residual thermal conductivity in the low-temperature limit, a theoretical explanation was provided in 2017 that topological insulators may be susceptible to form excitons or magnetoexcitons with an applied field [45]. The model utilizes the "Mexican hatlike" band structure with the lower band being completely filled up, and the formation of the exciton with a "ringlike" dispersion occurs when including a strong f-level interaction on top of the bands. To account for the observed residual term, the exciton binding energy is made large enough so that the exciton gap energy is smaller than the band gap. With this, the exciton can be modeled as a noninteracting boson gas, and the ringlike minimum would yield a constant κ/T. To account for the quantum oscillations, the charge-neutral magnetoexcitons form discrete Landau levels with an applied field which would allow quantum oscillations to be observed even in band insulators.

In 2018, Chowdhury et al. developed a “composite exciton Fermi liquid” model to explain the possible mechanism behind having a charge-neutral fermion with a 3D Fermi surface [46]. The basis of this two-band model is that a charge-neutral fermionic quasiparticle forms in a mixed-valence insulator under the limit of a strong Coulomb interaction. The model utilizes the particle-hole transformation of the f-electron where the f-electron valence fluctuates between 1 and 2, in which 1 is considered an “empty state” and 2 is a state with one hole. With the condition of an infinite Coulomb repulsion of the f-hole and a huge, but infinite, attractive interaction between the f-hole and the d-electron, the f-hole can be fractionalized into a spinless boson (or a “holon”) with a negative charge and a neutral fermion (“spinon”). Due to having this huge attractive interaction between the f-hole and the d-electron, an attractive interaction exists between the holons and the conduction electrons, which, if strong enough, could form bound states with each other to manifest a charge-neutral fermionic composite exciton. For a finite hybridization between the d- and the f-electrons and the hopping of the spinon, the composite exciton hybridizes with the spinon, which yields energy bands with a Fermi surface that has the characteristics of both the fermionic composite exciton and the spinon. Due to the screening and surface reconstruction, the attraction between the holon and the conduction electron weakens, allowing metallic quasiparticles to form on the surface.

The ambiguous nature of the experimental results from these studies regarding the Fermi surface could be due to the intrinsic differences within the samples. Such differences may be caused by the two different growth methods that are used to synthesize single crystal SmB_6 [1].

1.2 Floating-zone versus Flux Grown SmB_6

A 1981 study focused on $Sm_xM_{1-x}B_6$, where M is the ion of the divalent and trivalent metal, and metal deficient Sm_xB_6 [27]. The compositions of the whole crystal were found by using chemical and x-ray structural analysis and the individual grains by x-ray spectral analysis. It was discovered that when divalent rare-earth atoms with an atomic radius greater than samarium were introduced, the lattice constant of the boride increases, causing the effective valence to 3. Meanwhile, the introduction of the trivalent atom decreases the effective valence. There was no difference between magnetic elements and nonmagnetic elements. As such, the samarium vacancies enhance the samarium valence from nonmagnetic Sm^{2+} to $J = 5/2$ magnetic Sm^{3+} [27]. Not only that, the samarium vacancies of 1% concentration were found to break down the Kondo insulating behavior of SmB_6. [31]

There are two main growth methods for synthesizing single crystal SmB_6: floating-zone and flux method [1]. The floating-zone method starts with a polycrystalline SmB_6 feed crystal rod that is placed in an argon environment to prevent oxidation and goes through the "molten zone" that can reach up to ~2000°C, prompting crystal growth. The resulting single crystal rod has a varying lattice parameter along its length. Due to the high temperatures during the growth process, some of the samarium ions are vaporized, leaving samarium vacancies and introduction of some implicit strain. This method would allow the formation of crystals that are a few centimeters long.

The flux-grown method relies on the low melting point of aluminum and the solubility of the constituent elements. The samarium and boron powders, along with aluminum (with its function as the flux), are placed in a crucible, which is heated to ~1450 °C and then slowly cooled. Crystal growth occurs by nucleation from the molten aluminum during the cooling. Because flux-growth method is done under the melting point of the crystal, there are no samarium deficiencies when utilizing with this method, which may enhance the stoichiometry of the sample. However, flux-grown SmB_6 are known to contain epitaxially oriented aluminum inclusions with a similar lattice parameter, making the detection of these aluminum pockets with methods such as XRD much more difficult. Crystals yielded from this growth method are a few millimeters long [1].

In order to investigate the effects of the samarium vacancies, a 2019 study measured the magnetic susceptibility, electrical resistivity, Hall effect, and heat capacity of flux-grown SmB_6 with varying samarium-deficiencies [47]. This study was motivated by the contradictory results of doped SmB_6 between floating-zone and flux-grown samples, where the resistivity decreased with doping for floating-zone grown samples. Interestingly, there was no limiting value of the Sm^{3+} ions with more vacancies, which was unexpected as such a limiting value was expected due to the requirements that a samarium vacancy needs the 5d electrons from two Sm^{3+} ions. This observation would agree with the transport experiments that the carrier concentration decreases as the vacancies increase. The resistivity measurements were quite similar between all the samples, as all started to plateau around <5 K and have identical activation energies. Even though the vacancies would act as holes that would increase the conductivity, resistivity at low temperatures increased with higher vacancy due to the vacancies causing scattering that would impede hybridization. This impeded hybridization partially smears the hybridization gap in the bulk, weakening the spin-momentum locking. The energy gap seen in the Hall effect was not affected by the vacancies, though the Hall mobility under low temperatures was considered too high with just the conduction activated through hopping. One of the possibilities is that there may be conduction within the bulk, which was also noted due to the significant low-temperature fermionic heat capacity that only slightly decreased with doping. The study concluded that the overall properties had a minimal change but noted that because of these observations, SmB_6 might not be a perfect topological insulator.

Transport measurements between the two growth methods have yielded resistivity saturation with different features, as flux-grown SmB_6 have temperature-independent resistivity plateaus[43, 48, 49], while floating-zone SmB_6 has been shown to present a more inconsistent behavior [1, 50, 51]. Currently, ARPES measurements have shown evidence of a trivial surface state in floating-zone grown SmB_6 [52], while flux-grown SmB_6 have exhibited compelling characteristics in alignment with a topological surface [17]. Additionally, only floating-zone grown SmB_6 have exhibited a large residual density of states suggesting the possibility of charge-neutral fermions within the bulk [30], while so far, there has been no evidence of flux-grown SmB_6 hosting charge-neutral fermionic quasiparticles in the bulk [28, 29].

A 2021 study sought to investigate these differences by conducting electrical transport measurements on floating-zone grown SmB_6 using the inverted resistance method with a Corbino disk geometry [53]. The method allows the observation of the residual bulk conduction that would be dominated by the surface conduction at low temperatures under a typical electrical transport setup. The residual bulk conduction observed between the floating-zone grown samples were significant and varied by sample, while the flux-grown samples with samarium deficiencies demonstrated a truly insulating bulk. Contribution from the samarium deficiencies were considered, but because the bulk conduction was too large with just the samarium deficiencies, dislocations were also attributed to be the possible cause, with these dislocations being one-dimensional defects possibly originating from the internal stresses or impurities introduced during the growth processes. Chemical etching was used to observe the terminations of the dislocation on the surface via scanning tunnel microscopy, as the material is removed at a different rate near a defect during the etching process. It was observed that the flux-grown SmB_6 had a higher dislocation density compared to the flux-grown samples.

1.3 Application of Pressure and Strain

This section will focus on the more extrinsic view on SmB_6, with the aim being to lead the discussion to tunable parameters of the application of pressure and strain. In 2020, an explanation was proposed for the mixed-valence nature of the samarium ion [32]. The fluctuation of the samarium valence is due to the octahedral boron structure having a slight distortion. This is caused by the boron dimers having a temperature and pressure-dependent stretch and displacement, thus being pulled from the near center of the unit cell face towards one of the samarium ions. Due to the proximity of the boron dimer, the samarium ion is then able to transfer a single electron [32].

It was already known by 1970 that the application of pressure had been shown to cause the insulator-metal transition in SmS [5]. In 1994, Cooley et al. studied pressurized SmB_6, where it was discovered that the Kondo gap could be reduced and eventually discontinuously vanish with pressure, transitioning SmB6 into a metal [43]. They discovered that the activation energy was insensitive to magnetic fields up to 18T and did not observe a discontinuous valence change with the disappearance of the gap.

A 2018 study measured x-ray absorption spectroscopy (XAS) and x-ray magnetic circular dichroism (XMCD) spectra on floating-zone grown SmB_6 under temperatures down to 8K and pressures up to 26 GPa [54]. It was observed that samarium ions have a higher valence and a stronger magnetization at the 4f state at the surface compared to that in the bulk due to the reduction of screening by local moments and the hybridization between d- and the f-bands. Increasing the temperature increased the samarium valence of both the surface and the bulk. There was a rapid increase of the valence for both the surface and the bulk under pressure from 0.6 GPa to 8 GPa and a slower increase from 8 GPa to 26 GPa. This decrease in the rate correlated with the transition from a nonmagnetic insulator to a magnetic metal and is attributed to the loss of the 5d electron magnetization and an emergence of a more localized 4f state with higher valence in the samarium ions within the bulk. Another study conducted in the same year also measured XAS and XMCD spectra on floating-zone grown SmB_6 [55]. The study concluded that the net magnetic moment of Sm^{3+} ions was antialigned with the applied field, which is in contrast with the previous study stating that the Sm^{3+} ions aligned with the field due to the observation of a highly decreased 4f magnetization. This is due to the observation of a positive bulk magnetization at 2 K, which requires that the negative moment of the Sm^{3+} ions is not significant at the bulk. The provided explanation was that the antialignment emerges from the Sm^{3+} ions coupling antiferromagnetically with the moment of paramagnetic impurities, which would relieve the discrepancy with the previous study as this would make the XAS and XMCD studies dependent on magnetic impurities affecting the magnetic behavior of the Sm^{3+} ions.

High-pressure electrical transport measurements were conducted on SmB_6 up to 37 GPa the next year [61]. As the pressure was increased up to 10 GPa, the resistance decreased significantly with a vanishing plateau, indicating a transition from an insulator to a metal, and the observed negative peak in the Hall coefficient gradually flattened out to near zero, implying that the charge carriers decreased with pressure and that the bulk state has a conductance that is near that of the surface state. Their low-pressure data fitted well with the two-channel model composed of the temperature-independent surface state in parallel with the thermally activated bulk, while there were deviations in the higher pressure range after where the Hall coefficient originally had a peak under low pressure. The study notes that since the Hall coefficient was observed to be almost constant up to 37 GPa there is a robust long-ranged magnetically ordered state due to the pressure-induced valence increase of the samarium ions and the stable cubic lattice structure.

The question is if the application of compressive strain, equivalent to positive pressure, and tensile strain, analogous to negative pressure, would yield similarly expected behavior. This was tested in our group in 2017, where electrical measurements were performed on a strain apparatus that utilized a tri-piezo technique [33]. The application of the tensile strain has been shown to enhance the metallic state up to 240K with 0.7% strain along the <100> axis and persisted even after the strain was removed [33]. Although there is no comprehensive theoretical explanation for this phenomenon, it was thought that the strain affected the temporal and spatial fluctuations of f-electron configuration.

This dissertation will focus on the thermal transport experiments of SmB_6 and the concepts that will lead to the experiment involving the application of uniaxial tensile strain up to 0.27%.

Chapter 2

Equipment

In order to observe quantum behavior, it is necessary to reduce thermal fluctuations and atomic movements within the sample as much as possible. This is due to quantum mechanical effects involving interactions and energies on a scale that's much lower than those present under a typical atmospheric environment. Therefore, experiments are commonly performed under cryogenic temperatures and a high vacuum environment through the use of cryostats. There are various refrigeration technology options that allow cryogenic temperatures to be achieved, but this chapter will focus on the cryostats Quantum Design's Physical Property Measurement System, also known as the PPMS, and Oxford Instruments Kelvinox-MX 250 dilution refrigerator and superconducting magnet system. These two systems both utilize evaporation of liquid Helium-4, which by itself can achieve generally around 4.2K to 1.3K, but this range can be lowered further by incorporating an isotopic mixture of ^{3}He and ^{4}He [36]. The PPMS mainly uses only ^{4}He, though a ^{3}He insert can be utilized to reach down to a base temperature of 350 mK, while the Kelvin-MX 250 dilution refrigerator utilizes the isotopic helium mixture to achieve a base temperature of 70 mK. For the field, the superconducting magnet in the PPMS can apply 9T, and for the dilution fridge can supply up to 12T, though 14T is also possible with additional cooling to the magnet. A general description of the cooling method of both equipments will be outlined below.

2.1 Quantum Design PPMS

The PPMS has several built-in measurement options, such as electrical transport, magnetometry, and heat capacity. Due to a standardized puck design provided by Quantum Design, mounting the sample on the gold-plated copper puck is relatively easy and quick, allowing a high measurement turnover. The standard resistivity puck contains 12 electrical leads, thus having the capability of conducting a maximum of three four-probe conductivity measurements simultaneously. Experiments on the PPMS were conducted by utilizing the resistivity puck and a breakout box.

The puck is located within the sample chamber of the probe. The probe is immersed in the liquid helium bath inside the dewar and is made up of concentric stainless steel tubes. Within these concentric tubes is the sample chamber, with the first neighboring tube being the cooling annulus, next being the inner vacuum tube, a vacuum layer containing reflective superinsulation, an aluminum heat shield, an outer vacuum tube, and then the nitrogen jacket. The design is meant to insulate the helium bath as much as feasibly possible, resulting in significantly less helium consumption compared to having just a helium dewar. Additionally, the sample chamber also has a top-plate baffle assembly meant to aid in isolating the bottom of the sample chamber to the top, where there is heat being radiated by components that are at room temperature.

As the sample chamber itself is actually dry, cooling is done through the fingers of the puck, making direct thermal and mechanical contact with the walls of the sample chamber. At above 4.2K, the sample space is cooled by the cold helium vapor pulled through the impedance tube into the cooling annulus. Further cooling below 4.2K is done by pumping on the annulus, lowering the vapor pressure and cooling the bottom of the sample chamber to ~1.8K. Initial pumping is done through a vacuum pump located along the PPMS Model 6000 pumping line, but further pumping can be achieved by cryopumping via a charcoal sorption pump. To cool down to 350 mK, a ^{3}He insert assembly must be utilized as an addition to the PPMS. The concept regarding evaporative cooling via ^{3}He-^{4}He mixture will be explained in the next section, as the method is identical for both types of equipment, though accomplished through slightly different means in terms of hardware design.

Figure 2.1. Quantum Design PPMS fitted with a Cryomech HeRL15 helium reliquefier.

2.2 Oxford Instruments Dilution Refrigerator

The dilution fridge uses the heat of mixing of ^{3}He and ^{4}He isotopes to obtain temperatures that are much lower compared to other available refrigeration methods. However, even though the Kelvinox MX-250 dilution fridge (Figure 2.2) can achieve a base temperature of 70mK compared to 350mK on the PPMS, successive sample change takes nearly a month due to the time needed to reach the base temperature and to condense the helium vapor lost during the cooldown process. Therefore, the PPMS is ideal for use during the prototyping phase or to conduct preliminary measurements if the base temperature does not need to be lower than that of the dilution fridge.

2.2.1 Cooldown Procedure

The basic principle of the dilution fridge will be explained in this chapter, as the full description for the design of commercial dilution refrigerators is much more complex because it requires multiple shielding and heat exchangers. The general external configuration of the dilution fridge is very similar to the PPMS, with an outer vacuum chamber (OVC), the nitrogen jacket, a vacuum layer, the helium dewar (also known as the main bath), an inner vacuum chamber (IVC), and the sample space within the radiation shield. However, design-wise, this is where the similarities between the two systems end. The cooldown procedure happens in three stages, where it is first cooled to 77K via liquid nitrogen, then to 4.2K via liquid ^{4}He (these two steps are also the same as the PPMS), and lastly through condensing the ^{3}He/^{4}He mixture to reach all the way down to 70mK. The dilution unit is the space within the IVC, where the evaporative cooling will occur to it down to base temperature. It is part of a more extensive system that's connected to the ^{3}He/^{4}He circulation system, as shown through the Triton System Control program.

Figure 2.2 Kelvinox MX-250 dilution refrigerator fitted with a Cryomech HeRL15 helium reliquefier. The cryostat is set on a vibrationally isolated frame over a huge pit. This setup allows the helium dewar to be lowered, which would expose the IVC. The gas valve system on the left is part of the helium recovery system.

When the sample is loaded, the IVC is secured by stainless steel screws and sealed by indium wire, which is malleable and nonferrous and has been used for sealing in cryogenic temperatures. The IVC and helium dewar must then be pumped out and leak checked (accessible port shown on Figure 2.3 and 2.4), along with the charcoal traps being cleaned, pumped out, and cooled with liquid nitrogen (which will be explained later). Before cooldown, it is necessary to insert a small amount of helium gas into the dilution unit in order to establish thermal contact between the dilution unit and the helium dewar while being careful not to insert any air. For the cooldown to 77K, the nitrogen and helium dewar is pumped and flushed with nitrogen gas. The helium dewar is filled with helium gas, and the 1K pot (a separate chamber within the dilution unit) is filled with helium gas and pumped on for approximately a minute. Then the nitrogen dewar can be filled with liquid nitrogen, which will cool down the system to 77K.

To cool down the system to 4.2K, liquid nitrogen in the helium dewar is blown out to the nitrogen dewar by overpressurizing the helium dewar with nitrogen gas. Then the helium dewar is pumped and flushed by first nitrogen gas, then helium gas, and finished off with the helium dewar being filled with helium gas (as shown in Figure 2.3) and the 1K pot pumped for ~1 minute. Finally, liquid helium can be transferred to the dewar by a double-walled vacuum transfer tube, which should be pumped out for a few hours before the transfer. When the system has reached 4.2K, an isotopic mixture made of ^{3}He and ^{4}He can be condensed to cool down the system to base temperature. Most of this process can be done remotely by the Triton System Control program, as shown in Figure 2.5, which allows control of the gas valves and gives pressure readings along the ^{3}He/^{4}He circulation system. The actual pumps involved in the condensing process are shown in Figure 2.6. There are a few steps that have to be done manually, specifically opening up a few valves during the condensing process.

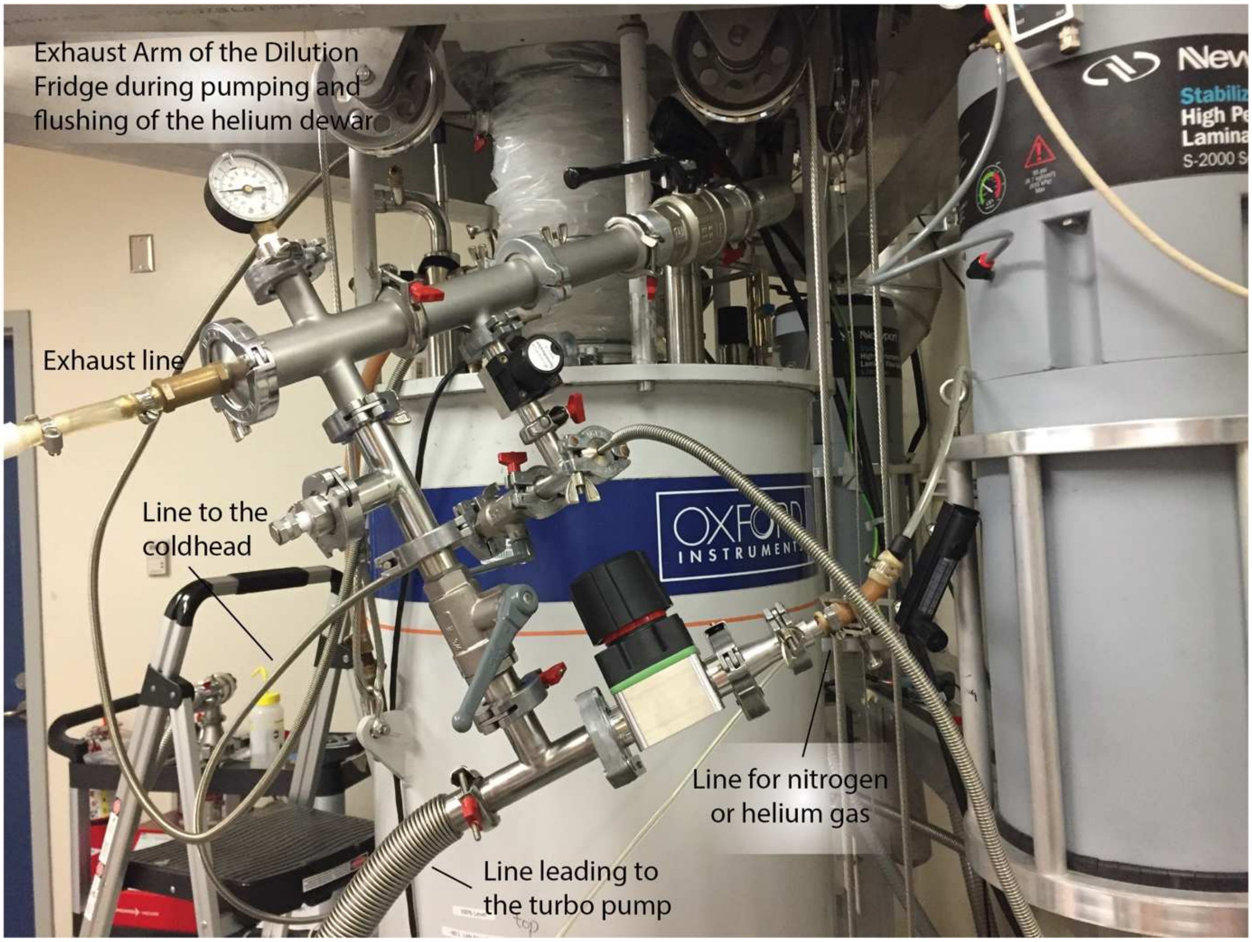

Figure 2.3. The exhaust arm of the dilution fridge during the pumping and flushing of the helium dewar. The exhaust arm is one of the access points to the helium dewar, though it is not used for liquid helium transfers but for gas transfers.

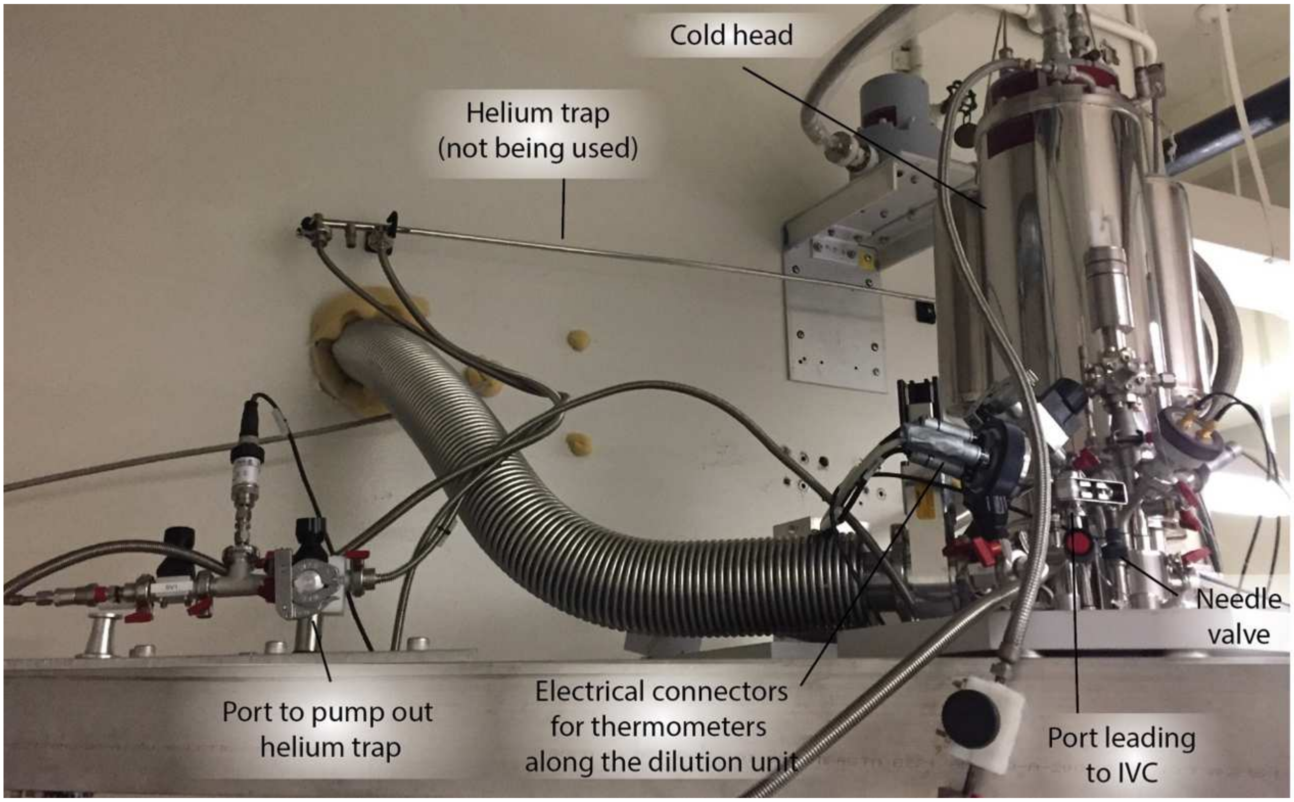

Figure 2.4. Top of the dilution fridge. The various ports and valves are available in this area and are for gas transfer, such as pumping out the helium trap and condensing the mixture.The electrical connectors measuring the thermometers along the dilution may have to be unplugged when inserting the helium trap.

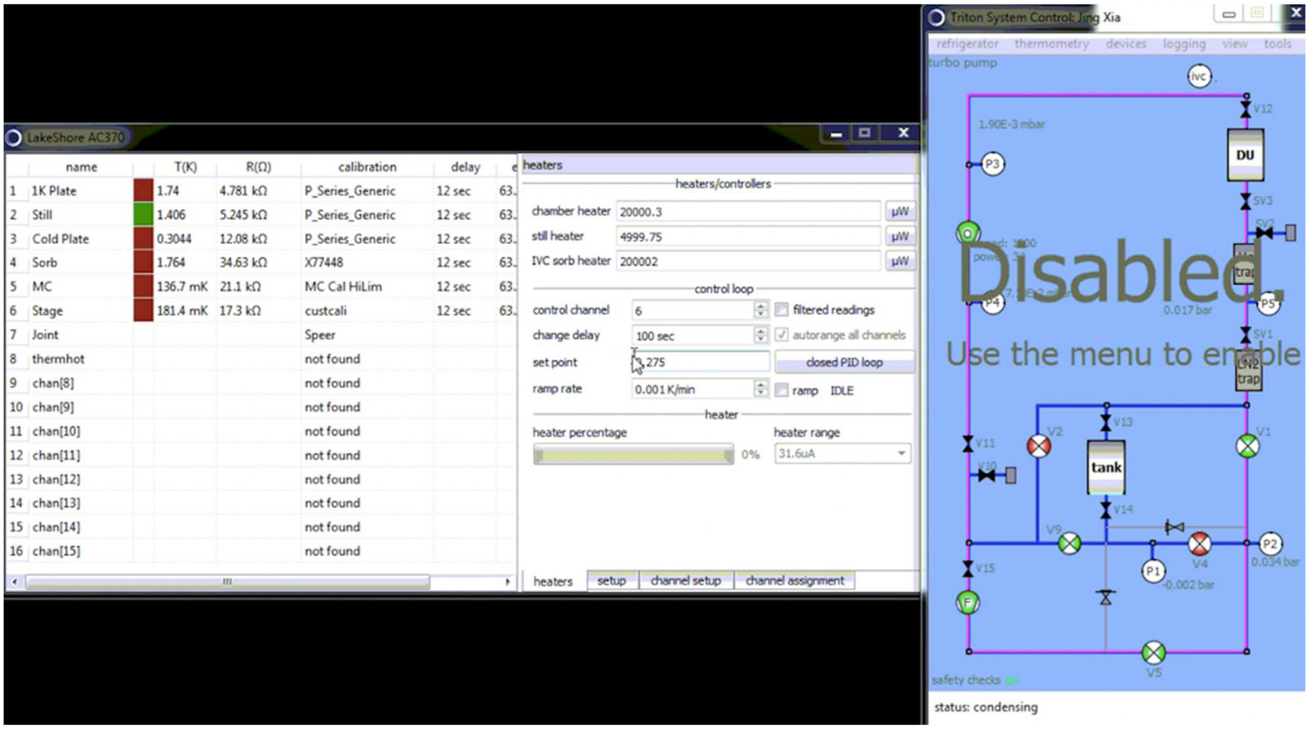

	name		T(K)	R(Ω)	calibration	delay	e
1	1K Plate	🟥	1.74	4.781 kΩ	P_Series_Generic	12 sec	63.
2	Still	🟩	1.406	5.245 kΩ	P_Series_Generic	12 sec	63.
3	Cold Plate	🟥	0.3044	12.08 kΩ	P_Series_Generic	12 sec	63.
4	Sorb	🟥	1.764	34.63 kΩ	X77448	12 sec	63.
5	MC	🟥	136.7 mK	21.1 kΩ	MC Cal HiLim	12 sec	63.
6	Stage	🟥	181.4 mK	17.3 kΩ	custcali	12 sec	63.
7	Joint				Speer		
8	thermhot				not found		
9	chan[8]				not found		
10	chan[9]				not found		
11	chan[10]				not found		
12	chan[11]				not found		
13	chan[12]				not found		
14	chan[13]				not found		
15	chan[14]				not found		
16	chan[15]				not found		

heaters

heaters/controllers

chamber heater 20000.3 μW
still heater 4999.75 μW
IVC sorb heater 200002 μW

control loop

control channel 6
☐ filtered readings
change delay 100 sec
☑ autorange all channels
set point 275
closed PID loop
ramp rate 0.001 K/min
☐ ramp IDLE

heater

heater percentage 0%
heater range 31.6uA

Disabled.
Use the menu to enable

status: condensing

Figure 2.5. Display showing the screen of remote operation during the mixure condensing proccess. The display on the left shows the various temperatures measured along different points of the dilution unit. The right shows the Triton System Control program that allows remote control of the forepump, gas valves V, and turbo pump as well as displaying the pressure measurements labeled P. The mixture is released from the tank by opening V9 and is being circulated as shown by the pink outline.

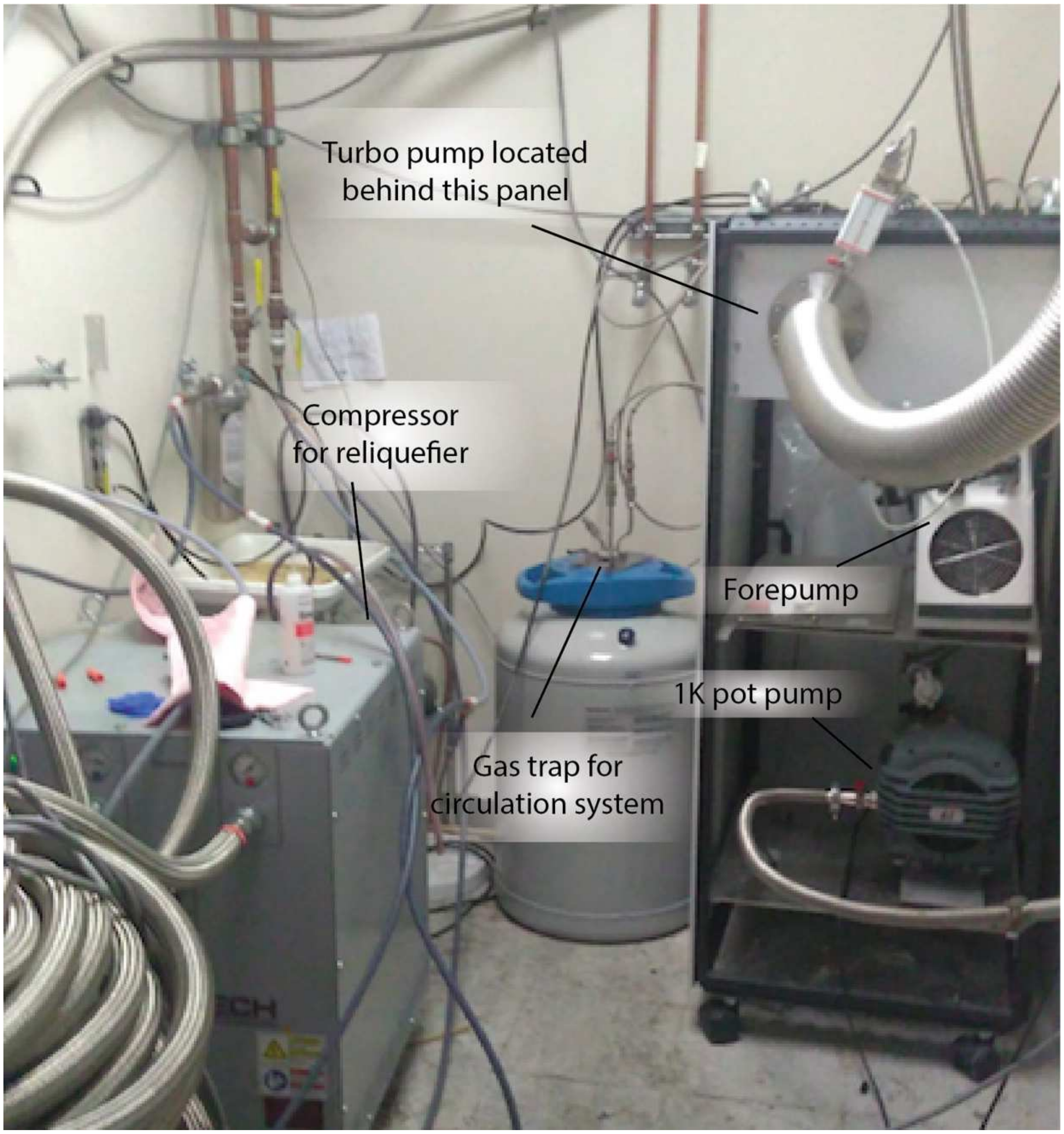

Figure 2.6. The “pump” room. The forepump and turbo pump can be controlled remotely while the 1K pot pump can only be accessed manually. The forepump pumps on the circulation system before the condensing process begins, while the turbo pump is used to further cool down to base. Also shown in this picture is the gap trap system for the circulation system and the compressor which is used for the reliquefier.

2.2.2 Condensing the ^{3}He/^{4}He Mixture

First, gas valve V5 is opened, and then the ^{3}He/^{4}He circulation system is pumped on by a forepump shown as “O” in Figure 2.5. Then a mixture for the ^{3}He and ^{4}He is pulled from a storage (or dump) vessel (also known as the “tank”) via opening up valve V9 and goes through a liquid nitrogen cooled charcoal gas trap. The mixture then goes through a smaller trap located in the helium dewar. These gas traps are used to absorb any impurities such as nitrogen, oxygen, and moisture from the atmosphere that were introduced through small leaks in the dilution unit. The mixture is precooled by the helium dewar and goes through the 1K pot (or plate) located within the dilution unit (“DU” on Figure 2.5), where it gets condensed. The 1K pot is where liquid ^{4}He gets pulled from the main bath and pumped on by a rotary pump known as the 1K pot pump. The flow rate of liquid ^{4}He is adjustable through the needle valve, allowing the cooling power to be controlled in the 1K pot, which typically reaches below 2K. After some further cooling through several heat exchangers, the mixture collects in the mixing chamber. In the mixing chamber, ^{4}He gas undergoes Bose condensation, becoming a superfluid, while ^{3}He atoms are Fermi particles and thus does not form a condensate (though there is a weakly attractive interaction between two ^{3}He atoms, which may cause pairing of the two atoms to collectively behave like bosons—however, this only occurs under 3mK) [36]. The mixing chamber is then cooled below 0.867K by reducing the vapor pressure of the liquid via the turbo pump. Phase separation of the mixture occurs below this temperature, which is known as the tri-critical temperature, as shown in Figure 2.7. The phase separation results in two distinct phases that co-exist: the “dilute” phase where a concentration of 6.6% ^{3}He exists as a Fermi liquid submerged in a superfluid ^{4}He (concentration 93.3%) and the “concentrated phase” made up of nearly 100% normal ^{3}He liquid. Due to its lower density, the ^{3}He-rich liquid floats on top of the ^{4}He-rich liquid in the mixing chamber, and the cooling occurs when the ^{3}He evaporates from the concentrated phase to the dilute phase. In order to ensure optimal cooling, the concentration of 3He and the volume of the mixture is carefully chosen so that the phase boundary is inside the mixing chamber. For a continuous operation under base temperature, ^{3}He has to be extracted from the dilute phase in order to be returned to the concentrated phase, hence why ^{3}He is circulated through the *circulation* system.

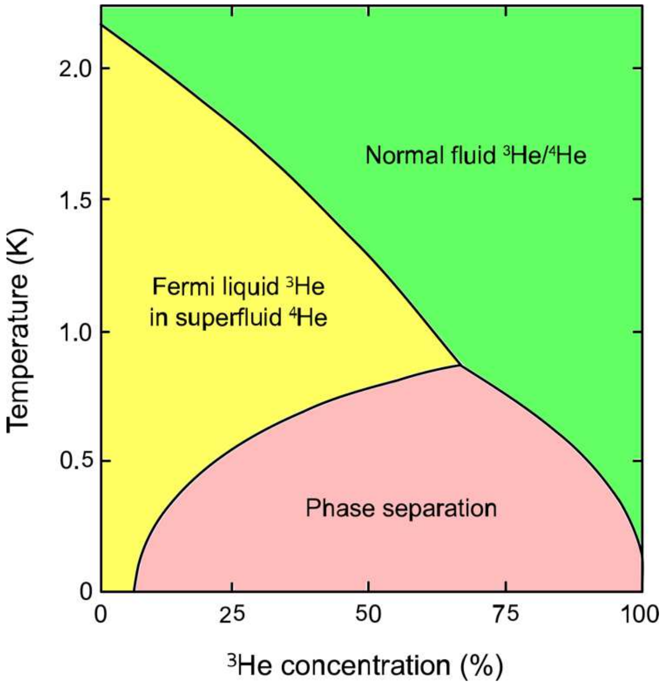

Figure 2.7. Phase diagram of ^{3}He/^{4}He mixture under saturated vapor pressure. The diagram shows two different phases of ^{3}He/^{4}He mixture, along with the parameters for where the mixture separates into two separate co-existing phases. The point in the parameter line bordering of all three regions is called the tri-critical temperature, which is ~0.86K. Figure based on reference [37] by Mets501 licensed under Creative Commons Attribution-Share Alike 3.0 Unported.

2.2.3 Sample Stage

There is no standardized sample stage for the dilution fridge; instead, the sample stage mount was custom-built with a plastic frame and silver foil for the thermal grounding, as shown in Figure 2.5. The initial design used copper but was found to produce eddy current heating during field sweeps and contributed a non-negligible amount of additional thermal conductivity. The pins of the dilution fridge stage are used to make electrical contact with the sample and any other components (such as thermometers) to the stage through the black square pin connectors. Thermal grounding to the stage can be accomplished by attaching silver foil via brass screws through the holes on the stage. The stage is mechanically secured by plastic screws on the plastic frame, while the thermal ground is provided via a silver foil from the stage screwed to a silver wire (the square brass piece provides more contact with the screw to the wire). The black square pin connectors of the stage are connected to those located along the sample stage mount, which is electrically connected to the breakout box.

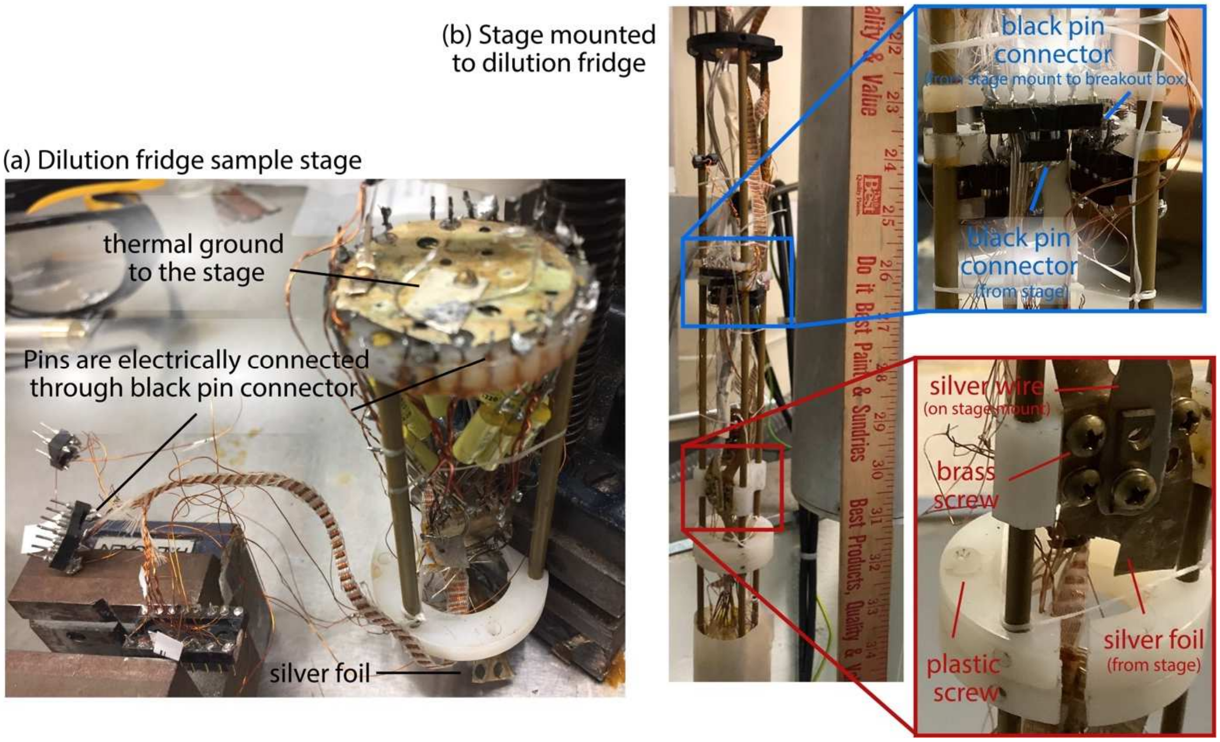

(a) Dilution fridge sample stage

(b) Stage mounted to dilution fridge

Figure 2.8 (a) Dilution fridge sample stage (b) that is mounted onto the diution fridge. The pins surrounding the flat portion of the stage (where the setup is placed) are used to electrically contact the components of the experimental setup.

2.3 Helium Recovery System

Helium is the only completely nonrenewable resource and is found in natural gas deposits. Due to the limited supply and the increasing demand for research and commercial purposes, the cost and the availability of helium can be quite unreliable. Because of this, the PPMS and the dilution fridge have been integrated into a helium recovery system, where the helium exhausted from both equipment will be stored in balloons, purified through an activated charcoal trap, then reliquefied back into the helium dewars.

2.3.1 Storage

The exhaust is stored in huge plastic balloons, which were chosen due to ease of use compared to utilizing pressurized tanks and regulators, though the helium does leak very slowly over time. Due to any possible leaks in the system, non-helium gases may be present within the recovery system. These impurities must be removed before being liquefied, or else the reliquefier will not function optimally. Instead, the cold head will be clogged, which can cause helium gas to vent out from the dewar, and thus the dewar will suffer a gradual loss (which would lead back to the balloon but may not liquefy the helium at a higher rate compared to the venting rate). To prevent this, an activated charcoal trap cooled by nitrogen gas is implemented on the line leading before the reliquefier.

2.3.2 Purification

Both charcoal traps (for the dilution unit and the recovery system) must be maintained properly. For the trap located along the dilution unit, different traps are alternated between each sample change (which is pumped out before being installed back to the dilution unit). For the trap in the recovery system, the impurities absorbed by the charcoal must be relieved every day if helium is being flowed into the reliquefier, or else there is a risk of the charcoal not absorbing any more impurities. This can be done by closing off the trap system from the dewar, opening up a path where the impurities can be removed (usually a bag is attached to where the gas can be released in order to quantify how “dirty” the trap was), heating up the charcoal trap, pumping out the trap system, and filling it back up with helium gas before being reintroduced back into the system. Extra precaution is made even before the trap in the recovery system by implementing a drierite trap to capture the moisture. Daily cleaning of the charcoal trap for the recovery system and maintaining fresh drierite are a part of the general maintenance for upkeeping the dilution refrigeration system. In addition, the nitrogen dewar from the dilution fridge, the PPMS, and all the charcoal traps should be refilled with liquid nitrogen every few days.

2.3.3. Clogs

The cold head may become clogged if the system has a leak, in which the helium reliquefier may be contaminated with either air or moisture. A clog may be present when high pressure is detected in the helium dewar even with the cold head heater being off , the compressor on, and there is nothing else that could be causing an increased heat load (such as condensing the mixture, field sweeps, or loading the helium trap). The procedure for unclogging the cold head is dependent on the type of clog. For an air clog, the cold head will be warmed up to 100K, causing the clog to be pushed out of the cold head by increasing the pressure of the helium gas. In the case of a water clog, the cold head will have to be warmed up to 300K, warranting a sample change procedure.

2.3 Superconducting Magnet

Magnetic fields are applied through the use of a superconducting magnet, which is operated in liquid helium at 4.2K. Up to 9 Tesla can be applied on the PPMS and 12 Tesla for the dilution fridge, though this can improve up to 14 Tesla with further cooling. The main advantage of using a superconducting magnet is its ability to operate under "persistent mode." During this operation, the superconducting circuit is closed to a continuous loop. This mode does not need continuous power; hence there is no need for a continuous power supply.

The Mercury IPS is the power supply for the dilution fridge magnet. When the magnet just has been cooled, it must be first be "trained" by operating under the "Slow" rate. The magnet will function properly only if all the conductors remain at a superconducting state. If any of the windings become resistive, the current will cause ohmic heating. If the ohmic heating is large enough, then all the stored energy in the magnet will dissipate, causing the liquid helium to rapidly evaporate and warm the magnet above 4.2K. This situation is called a quench.

In order to prevent a quench from occurring, the Mercury IPS monitors the helium level by reading the resistance of the helium probe that is inserted in the helium dewar. When attempting to operate the magnet with a low helium level, the Mercury IPS will detect the insufficient amount of helium and halt the operation of the magnet. The halting process looks like this: the user sets the desired field, and the magnet goes under Persistent mode; however, the field will not increase at all, instead prompting the magnet out of Persistent mode. If the dewar is full of helium and the Mercury IPS still halts the operation of the magnet, this could mean that there is something wrong with the helium level monitoring system. There may be an issue with the probe, the wire connections, the Mercury IPS, and/or the helium level card that is inside the Mercury IPS.

Chapter 3

Thermal conductivity of SmB_6

Before measuring the thermal conductivity of any sample, it is first ideal to have some quantitative relation to actual measurable quantities. In this chapter, the thermal conductivity will be derived for the experimental applications of SmB_6, then the experimental setup for typical thermal conductivity measurements will be introduced. Lastly, I will explain the features of SmB_6 that may be the possible causes of the experimental discrepancy observed with thermal conductivity and quantum oscillation measurements.

3.1 General Description

Heat transfer via conduction occurs through the movement and collision of energy carriers within a material. In solids, the principal energy carriers are the free electrons and phonons, or the quanta of lattice vibrations. The thermal conductivity of both energy carriers will be derived, with the focus being placed on utilizing these expressions for experimental applications of thermal conductivity measurements under low temperatures.

Let's consider a solid with a cross-sectional area of A and a thickness of X placed in between two large parallel plates. The temperature of the solid is at a constant T_0 throughout the whole material. Then the temperature of one of the plates is slightly increased to T_1 and stays at that temperature. Eventually there will be a linear steady state temperature distribution, in which there will a constant rate of heat flow J through the material maintaining the temperature difference $\Delta T = T_1 - T_0$. For small ΔT:

$$\frac{J}{A} = \kappa \frac{\Delta T}{X} \tag{1}$$

κ is the thermal conductivity, a proportionality constant that measures the material's ability to transfer heat. Equation (1) can be written in differential form:

$$\frac{J}{A} = -\kappa \frac{\partial \mathrm{T}}{\partial \mathbf{x}} \tag{2}$$

where the negative sign represents the heat flow from the hotter end of the material, or the negative of the temperature gradient, along the positive x-direction. This form suggests that the thermal energy transfer is a random process where the energy diffuses through the material and goes through frequent scattering. If the energy was going through the material without any deflection, then the expression would not depend on the temperature gradient but rather the difference in temperature ΔT [37,38].

The thermal current density can be found by considering a particle current of N particles with average velocity v. Integrating over all angles of the flux through some artibrary surface normal to the flux yields $\frac{1}{6}N\ v$ and the average thermal energy is $\frac{3}{2}k_B T$ per particle of a monatomic gas, thus the net thermal energy flux per unit area is

$$\frac{J}{A} = \frac{1}{6}N\ v\ \frac{3}{2}k_B\ \Delta T \tag{3}$$

Heat transfer occurs after an inelastic collision, where the particle traversed at a distance of the mean free path ℓ. The gradient is $\frac{\partial \mathrm{T}}{\partial \mathbf{x}} = \frac{T_1 - T_0}{2\ell}$, with the factor 2 accounting for the collisions in the opposite direction. Inserting the classical expression for the specific heat of a monatomic gas per unit volume $c_V = \frac{3}{2}Nk_B$, the thermal conductivity is

$$\kappa = \frac{1}{3}c_V v\ell \tag{4}$$

Next, a more explicit expression for the phonon and the electron contributions to the thermal conductivity will be shown using Equation (4), with the main consideration being that phonons are bosons and electrons are fermions. These contributions are additive

$$\kappa = \kappa_{electron} + \kappa_{phonon} \tag{5}$$

The focus will be to express these thermal conductivities for low temperatures, as this is the experimental temperature range of interest. Distinguishing the temperature limits allows a few approximation to be made.

The Debye model estimates the phonon contribution to the specific heat in a solid by treating each acoustic phonon mode as a quantized harmonic oscillator, with sound waves following the linear dispersion relation

$$\omega = v_s k \tag{6}$$

where ω is the phonon frequency, v_s is the sound velocity, and k the magnitude of the wavevector. The vibrational frequencies are set to equal to the number of classical degrees of freedom. The maximum frequency that limits the number sound wave modes in the system to $3N$, where N is the number of total modes, is the Debye frequency ω_D

$$3N = \int_0^{\omega_D} \omega\, D(\omega) \tag{7}$$

$D(\omega)$ is the phonon density of states per branch, which is defined as

$$D(\omega) = \frac{dN(\omega)}{d\omega} = \frac{d}{dk}\left(\frac{\frac{4}{3}\pi k^3}{\left(\frac{2\pi}{L}\right)^3}\right)\frac{dk}{d\omega} = \frac{V\omega^2}{2\pi^2 {v_s}^3} \tag{8}$$

where $N(\omega)$ can be found by dividing a sphere of k-space by a volume of the smallest magnitude of the wavevector $\frac{2\pi}{L}$, $\frac{dk}{d\omega}$ can be found by utilizing the linear dispersion relation, and the volume occupied by each mode is $V = L^3$.

Solving Equation (7) would yield the expression for the Debye frequency

$$\omega_D = \left(6\pi^2 \frac{N}{V}\right)^{1/3} v_s \tag{9}$$

which can be used to express Equation (8) in terms of ω_D. The Debye temperature is defined as

$$k_B \Theta_D = \hbar\omega_D \tag{10}$$

κ_{phonon} will be expressed in terms of Θ_D since the Θ_D has been measured for SmB_6 to be 373 K [39].

The expectation energy as a function of temperature is

$$\langle E\rangle = 3\int_0^{\omega_D} d\omega\, D(\omega)\, \hbar\omega(n_B(\omega)+1/2) \;= 3\int_0^{\omega_D} d\omega\, \left(\frac{V\omega^2}{2\pi^2 {v_s}^3}\right)\; \hbar\omega\left(\frac{1}{e^{\hbar\omega/(k_B T)}-1}+1/2\right) \quad (11)$$

where the factor of 3 accounts for the three polarizations for the acoustic phonons, $n_B(\omega)$ the Bose occupation number, and the ½ account for the zero point energy, which has no contribution to the heat capacity. Considering only the temperature dependent component (thus disregarding the ½ term as it will yield a temperature independent term), assuming the phonon velocity is independent of the polarization, and setting $x_D \equiv \Theta_D/T$ yields

$$\langle E\rangle = 9Nk_B T\left(\frac{T}{\Theta_D}\right)^3 \int_0^{x_D} dx\, \frac{x^3}{e^x-1} \quad (12)$$

In the low temperature limit, the upper bound of the integral can be set to infinity since for large T, $n_B(\omega)$ quickly goes to 0 well below ω_D. The integral then can be reduced to a Riemann zeta function, yielding $\pi^4/15$. Thus, the phonon contribution of heat capacity per unit volume at low temperatures is

$$c_V = \frac{1}{V}\frac{\partial\langle E\rangle}{\partial T} = \frac{12\pi^4}{5}\frac{N}{V}k_B\left(\frac{T}{\Theta_D}\right)^3 \quad (13)$$

The sound velocity can be expressed in terms of Θ_D

$$v_s = \frac{k_B\Theta_D}{\hbar}\frac{1}{\left(6\pi^2\frac{N}{V}\right)^{1/3}} \quad (p)$$

The term $n = \frac{N}{V}$ is the number density of SmB$_6$, which is $n = a^{-3}$ (where $a = 4.133$ Å for SmB$_6$) . This allows the sound velocity of SmB$_6$ to be calculated to be 5179 m s^{-1}.

Using Equations (4), (13), and (14) gives the expression for the phonon thermal conductivity

$$\kappa_{phonon} = \frac{2}{15}\pi^2 k_B \left(\frac{k_B T}{\hbar}\right)^3 v_s{}^{-2} \ell \tag{15}$$

As T → 0, the phonon mean path is only limited by the sample dimensions, thus the mean free path is $\ell = 2\sqrt{A/\pi}$, where A is the cross-sectional area of the sample. It is important to note that this expression is only valid for scattering off on rough sample surfaces, since smooth surfaces will cause specular reflections, which will cause the mean free path to have some power dependence of temperature. Therefore, with specular reflections, the mean free path will exceed the dimensions of the sample. Equation (15) will be used to estimate the experimental values of the phonon thermal conductivity [40].

The electron contribution will be calculated for the thermal conductivity using the free electron model. One has to be mindful of electrons being fermions, thus following the Pauli exclusion principle and the Fermi-Dirac distribution function. Every fermion occupies a unique quantum state, and the energy of the highest occupied quantum state at absolute zero temperature is known as the Fermi energy $\epsilon_F = \frac{\hbar^2}{2m} k_F{}^2$, where m is the mass of the electron and k_F is the wavevector at the Fermi surface, or the surface where ϵ_F is located in k-space. The Fermi energy can also be defined as the chemical potential at absolute zero, as the Fermi-Dirac distribution function changes discontinuously from 1 to 0, or the filled state suddenly changing to an empty state.

There can only be one unique set of wavevector components k_x, k_x, k_z for every volume element $(2\pi/L)^3$ in k-space. The number of orbitals in a sphere with volume $4\pi k_F{}^3/3$ is

$$N = 2\frac{4\pi k_F{}^3/3}{(2\pi/L)^3} = \frac{V}{3\pi^2} k_F{}^3 \tag{16}$$

The factor of 2 accounts for the two quantum states associated with the two distinct spins of an electron. The expression for k_F can be obtained using Equation (16) which then can be used to relate ϵ_F with the electron concentration $\frac{N}{V}$

$$\epsilon_F = \frac{\hbar^2}{2m}\left(\frac{3\pi^2 N}{V}\right)^{2/3} \tag{17}$$

The density of states, or the number of orbitals per unit energy, is

$$D(\epsilon) = \frac{dN}{d\epsilon} = \frac{V}{2\pi^2}\left(\frac{2m}{\hbar^2}\right)^{3/2} \epsilon^{1/2} = \frac{3N}{2\pi^2} \tag{18}$$

The density of states is normalized so that

$$N(T = 0) = \int_0^{\epsilon_F} d\epsilon\, D(\epsilon) = \int_0^{\infty} d\epsilon\, D(\epsilon) f(\epsilon) = N(T \neq 0) \tag{19}$$

With this, the expression for the electronic heat capacity per unit volume at low temperatures $k_B T \ll \epsilon_F$ can be derived. The total energy of a system of N electrons is

$$U = \int_0^{\infty} d\epsilon\, \epsilon\, D(\epsilon)\, f(\epsilon, T) \tag{20}$$

where $f(\epsilon, T)$ is the Fermi-Dirac distribution function. The heat capacity per unit volume is then

$$c_V = \frac{1}{V}\frac{\partial U}{\partial T} = \frac{1}{V}\int_0^{\infty} d\epsilon\, \epsilon\, D(\epsilon)\, \frac{df(\epsilon,T)}{dT} \tag{21}$$

which can be rewritten as

$$c_V = \frac{1}{V}\int_0^{\infty} d\epsilon\, (\epsilon - \epsilon_F)\, D(\epsilon)\, \frac{df(\epsilon,T)}{dT} \tag{22}$$

This can be done since Equation (22) fulfills the condition of Equation (19) and $f(\epsilon, T)$ is the only temperature-dependent term.

Because the focus is on low temperatures for which $k_B T \ll \epsilon_F$, the temperature dependence of the chemical potential can be disregarded, and instead can be set to equal to the Fermi energy. Furthermore, since $\frac{df(\epsilon,T)}{dT}$ is large at energies that lie close to the Fermi energy, $D(\epsilon)$ may be approximated at the Fermi surface to become a constant $D(\epsilon_F)$. Setting $\mathcal{B} \equiv \frac{1}{k_B T}$ and $x \equiv \mathcal{B}(\epsilon - \epsilon_F)$, the heat capacity per unit volume is

$$c_V = \frac{1}{V} {k_B}^2 \, T \, D(\epsilon_F) \int_{-\epsilon_F \mathcal{B}}^{\infty} dx \, x^2 \, \frac{e^x}{(e^x+1)^2} \tag{23}$$

For $k_B T \ll \epsilon_F$, the lower limit can be set to negative infinity. Solving the integral yields

$$c_V = \frac{\pi^2}{2} n k_B \frac{T}{T_F} \tag{24}$$

where n is the electron number density and Fermi temperature T_F follows the relation $\epsilon_F = k_B T_F$. With $\epsilon_F = \frac{1}{2} m {v_F}^2$,where Fermi velocity $v_F = \frac{\hbar k_F}{m}$, and the mean free path $\ell = v_F \tau$, where τ is the time between collisions, the expression for the electron contribution of the thermal conductivity can be evaluated to be

$$\kappa_{electron} = \frac{1}{3} c_V v_F \ell = \frac{\pi^2 n {k_B}^2 \tau}{3\, m} T \tag{25}$$

For metals, there is a connection between thermal conductivity and the electrical conductivity $\sigma = \frac{ne^2\tau}{m}$, as the free electrons are involved in both heat and electrical transport.

The Wiedemann-Franz Law states that the ratio between the thermal conductivity and electrical conductivity

$$\frac{\kappa_{electron}}{\sigma} = \frac{\pi^2}{3}\left(\frac{k_B}{e}\right)^2 T \tag{26}$$

where the constant of proportionality is independent of the type of metal. This is known as the Lorenz number $L_0 = \frac{\pi^2}{3}\left(\frac{k_B}{e}\right)^2 = 2.45 \times 10^{-8}$ W Ω/deg^2. The Wiedemann-Franz law is used for SmB_6 thermal conductivity measurements to approximate the thermal conductivity contribution from the metallic surface state [28–30].

The derivations for the phonon and electron thermal conductivities show that $\kappa_{phonon} \propto T^3$ and $\kappa_{electron} \propto T$. For thermal conductivity measurements, the thermal conductivity $\kappa(T)$ may be expressed as κ/T so that the electron contribution is a constant

$$\kappa/T = \kappa_{electron}/T + \kappa_{phonon}/T = \alpha + \beta T^2 \tag{27}$$

Using the free electron model for α yields a value close in magnitude with the experimental values, but it may deviate due to interactions of the conduction electrons with the periodic potential, phonons, or other conduction electrons.

There has been recent interest with measuring the thermal conductivity of SmB_6 due to recent studies suggesting a possibility of charge neutral fermionic excitations [25,30]. Because of the charge neutral nature of these excitations, electrical measurements would not work, thus quantum oscillation and thermal conductivity measurements have been the main methods for probing possible charge neutral fermions. The Wiedemann-Franz Law shows that for SmB_6, electrons have a negligible contribution, so if there are charge neutral fermions, they would emerge as a residual term of κ/T. However, with the currently available thermal conductivity studies on SmB_6, the existence of charge neutral fermionic excitations are inconclusive.

3.2 Experimental Setup

3.2.1 Introduction

An ideal experimental setup for measuring the thermal conductivity is the one that minimizes the heat loss of the experiment to the surrounding environment. This means that the experimental setup should be isolated from the surrounding environment while having a strong thermal contact between the individual components making up the experiment. In order to fulfill these conditions, measurements are performed under high vacuum, and all the contacts on the stage to be thermally insulated with the exception to the thermal grounding wire. The thermal conductivity κ relies on the factor $\frac{X}{A}$ from equation (1), where X is the distance between the two points of where the temperature is measured and A is the cross-sectional area of the sample. In order to reduce the measurement error when getting κ, $\frac{X}{A}$ should be as large as possible; hence for thermal conductivity measurements, it is ideal to use samples that are needle-shaped.

A diagram depicting a typical setup for measuring the thermal conductivity along with the actual setup is shown in Figure 3.1. Generally, thermal conductivity measurements have a setup that is analogous to the four-probe method for measuring the electrical impedance. The sample has four contacts made on the surface. The outer two ends are meant to inject a heat current from one end of the sample by using an ohmic heater and drain the heat current to the other end leading to a thermal ground, which is usually thermally linked to the sample stage or the mixing chamber. The two inner contacts are for the thermometers that will measure the temperature gradient. This setup would generate a steady-state temperature gradient lengthwise along the crystal that is measurable with the appropriate thermometer.

3.2.2 Contacts

Contacts are typically made with platinum or silver wires due to their high thermal conductivity under the temperature range of interest. Additionally, for high sensitivity measurements, it is crucial for contacts to have low electrical resistance. The Wiedemann-Franz law can be used to estimate the thermal conductivity of a contact by the contact's electrical resistance. Silver (H20E) epoxy or indium solder is used to make electrical and thermal contacts between the sample and the components involved with the thermal transport. Indium solder is critical for measurements under 8K due to the superconducting transition of the Pb/Sn solder and its relatively high quenching field required to re-establish strong thermal contact. Indium solder is suitable for low-temperature measurements due to the lower critical temperature and thus lower critical field. The thermal components that make electrical contact with the stage use manganin wires indium soldered to the pins of the stage. Manganin wires are poor thermal conductors, which makes it ideal to thermally isolate the experimental setup.

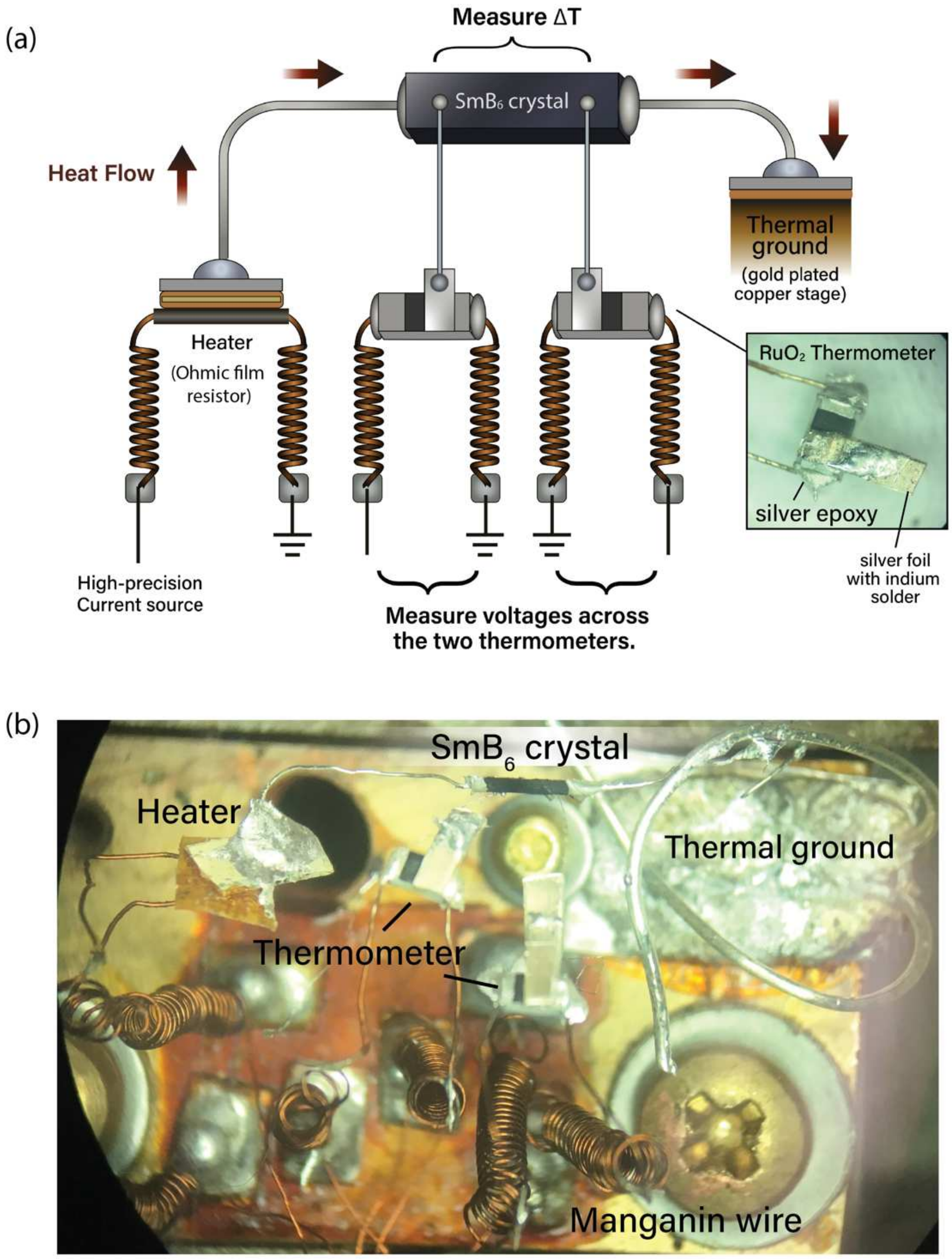

Figure 3.1. Typical setup for measuring the thermal conductivity. (a) Diagram of the setup illustrating the general components and the heat flow. Heat current is generated by applying current to the ohmic film resistor. It travels through the length of the sample and drains to the thermal ground. (b) The image of the stage with the experimental setup. The stage is used for the Janis dry (cryogen-free) cryostat, but the same concept applies for both the PPMS and the dilution fridge.

3.2.3 Thermometers

The thermometers are made of ruthenium oxide (RuO_2 or ROX) films mounted on a thick alumina substrate. These Vishay 732Ω thick film resistor thermometers are utilized due to their high sensitivity in cryogenic temperatures (viable from <1K down to a few millikelvin [36]), being able to detect down to a resolution of a few millikelvins. However, they do need to be thermally cycled before being implemented into the experimental setup, as there is a hysteresis of the electrical resistance in respect to the temperature. This hysteretic behavior is caused by some internal stresses within the alumina substrate, which can be relieved by thermally cycling the thermometers. Thermal cycling can be done by submerging the thermometers in liquid nitrogen and letting them warm up to room temperature, with this step being repeated ~40 times to assure a high degree of resistance reproducibility. Due to the thermometers being sensitive to temperature, exposure to hot temperatures, such as from the application of solder, can damage the thermometers, making them unusable. Therefore, the contacts that are placed directly on the thermometers are made with silver epoxy. However, using silver epoxy for all contacts will make the reusability of the components difficult. Utilizing indium solder allows easy reapplication of the contacts, but the hot solder should not be directly applied to the thermometer. Instead, a thin silver foil with a spot of indium is mounted on top of the thermometer via silver epoxy. The indium spot can be used to make contact with either silver or platinum wires connected to the sample. This process should be done quickly as possible in order to prevent warming up the thermometers too much.

3.2.4 Calibration

Since the thermometers are film resistors, they measure the voltages along the lock-in amplifiers that are electrically connected across the thermometers. In order to properly convert these voltages to temperature on the sample, the voltage readings are calibrated to the temperature reading of the stage thermometer, which has already been previously calibrated to the dilution fridge. Due to the slight hysteretic behaviors of the thermometers, the calibration must be performed in-situ. During the calibration phase, there will be no application of heat current through the heater. Instead, the temperature of the whole sample space will be changed by the still heater, as shown in Figure 3.2 (located within the IVC). Once the sample space is thermally equilibrated, the temperature of the stage thermometer would be very close to that of the two thermometers. However, having a high setpoint may cause a pressure high enough that the turbo pump, labeled as O in Figure 3.2, could be overexerted as indicated by the power. In this situation, the Triton system would automatically deactivate the turbo pump, which would require the mixture to be recondensed if not reactivated fast enough. In order to prevent this, the mixture is put back into the tank by activating valve V4 until the appropriate power (generally <95 on the Triton system since there is a risk of deactivation above this value). The still heater excitation is incremented at time intervals that are long enough for both thermal equilibration and a period of stable measurement to occur, which is approximately one to two hours per step. Each step is time-averaged, giving a single voltage value of each thermometer correlating to the temperature of the stage thermometer.

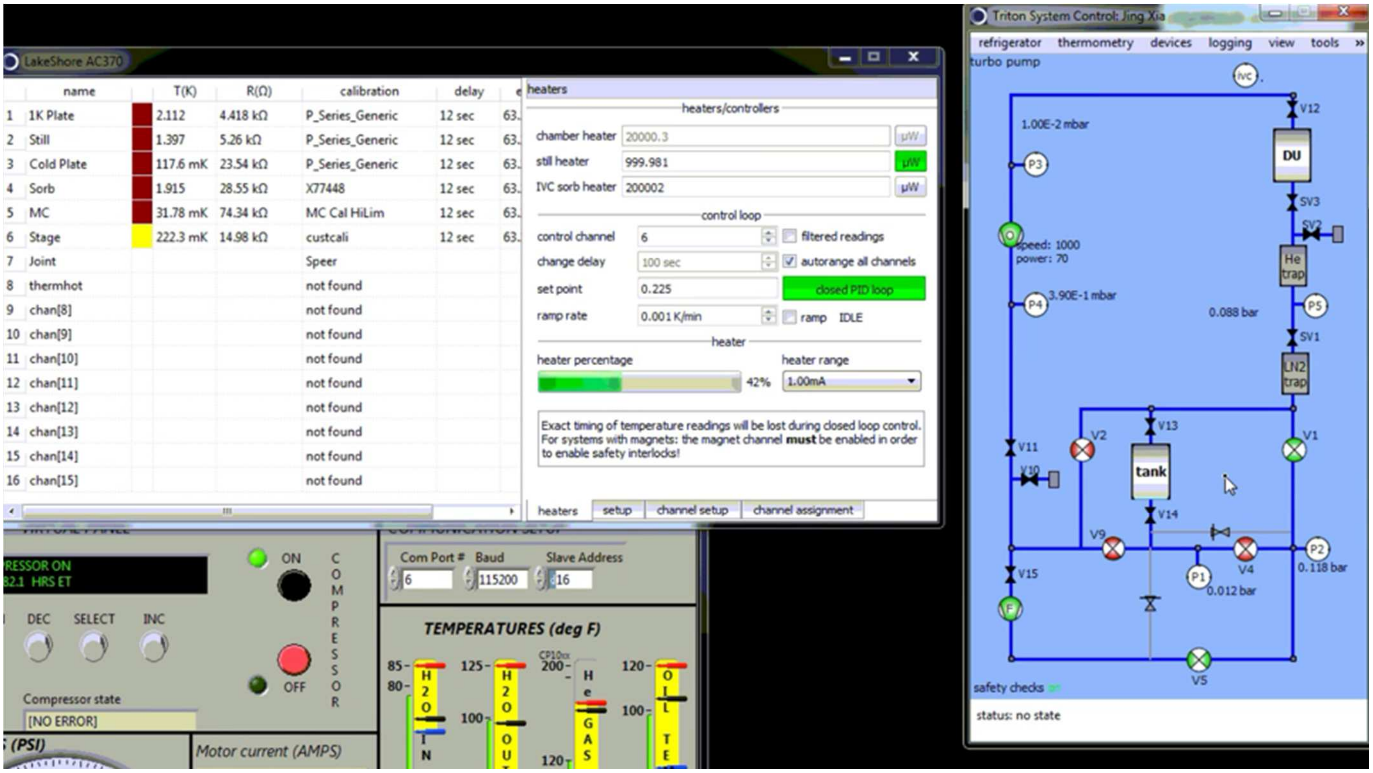
LakeShore AC370

	name		T(K)	R(Ω)	calibration	delay	e
1	1K Plate	🟥	2.112	4.418 kΩ	P_Series_Generic	12 sec	63.
2	Still	🟥	1.397	5.26 kΩ	P_Series_Generic	12 sec	63.
3	Cold Plate	🟥	117.6 mK	23.54 kΩ	P_Series_Generic	12 sec	63.
4	Sorb	🟥	1.915	28.55 kΩ	X77448	12 sec	63.
5	MC	🟥	31.78 mK	74.34 kΩ	MC Cal HiLim	12 sec	63.
6	Stage	🟨	222.3 mK	14.98 kΩ	custcali	12 sec	63.
7	Joint				Speer		
8	thermhot				not found		
9	chan[8]				not found		
10	chan[9]				not found		
11	chan[10]				not found		
12	chan[11]				not found		
13	chan[12]				not found		
14	chan[13]				not found		
15	chan[14]				not found		
16	chan[15]				not found		

heaters

heaters/controllers

chamber heater 20000.3 μW

still heater 999.981 μW

IVC sorb heater 200002 μW

control loop

control channel 6 ☐ filtered readings

change delay 100 sec ☑ autorange all channels

set point 0.225 closed PID loop

ramp rate 0.001 K/min ☐ ramp IDLE

heater

heater percentage 42%

heater range 1.00mA

Exact timing of temperature readings will be lost during closed loop control. For systems with magnets: the magnet channel **must** be enabled in order to enable safety interlocks!

Com Port # 6

Baud 115200

Slave Address 16

Compressor state [NO ERROR]

Triton System Control: Jing Xia

status: no state

Figure 3.2 Display of the calibration procedure. During the calibration procedure, the still heater is used to set the temperature of the stage while the voltages of the thermometers attached to the sample are measured. The still heater can be activated by choosing the "set point" temperature and switching on the closed PID loop. Possible high pressure on the dilution system due to the setpoint being too high may cause overexertion to the turbo pump, labeled O, which can be mitigated by flowing some of the mixture back into the tank via opening valve V4.

Figure 3.3 shows the data collected during the calibration procedure showing the voltages of the sample thermometers and the temperature of the stage, in which only the region where all three are equilibrated are averaged. Once the measurement for the calibration is done, the actual thermal conductivity experiment can be conducted by applying heat provided by the high precision current source to the sample heater. Figure 3.4 shows the data collected during the thermal transport measurement, which shows the voltages of the thermometers and the sample heater that will be used to calculate the thermal conductivity.

These thermometer voltages are then interpolated to the corresponding calibration measurement by using the cublic spline interpolation with a setting of a not-a-knot boundary condition so that the third derivative of the connecting splines are continuous. This process would allow the thermometer voltage of the thermal transport measurements to be converted into temperature by using the calibration data, which will be used to get the temperature gradient along the sample.

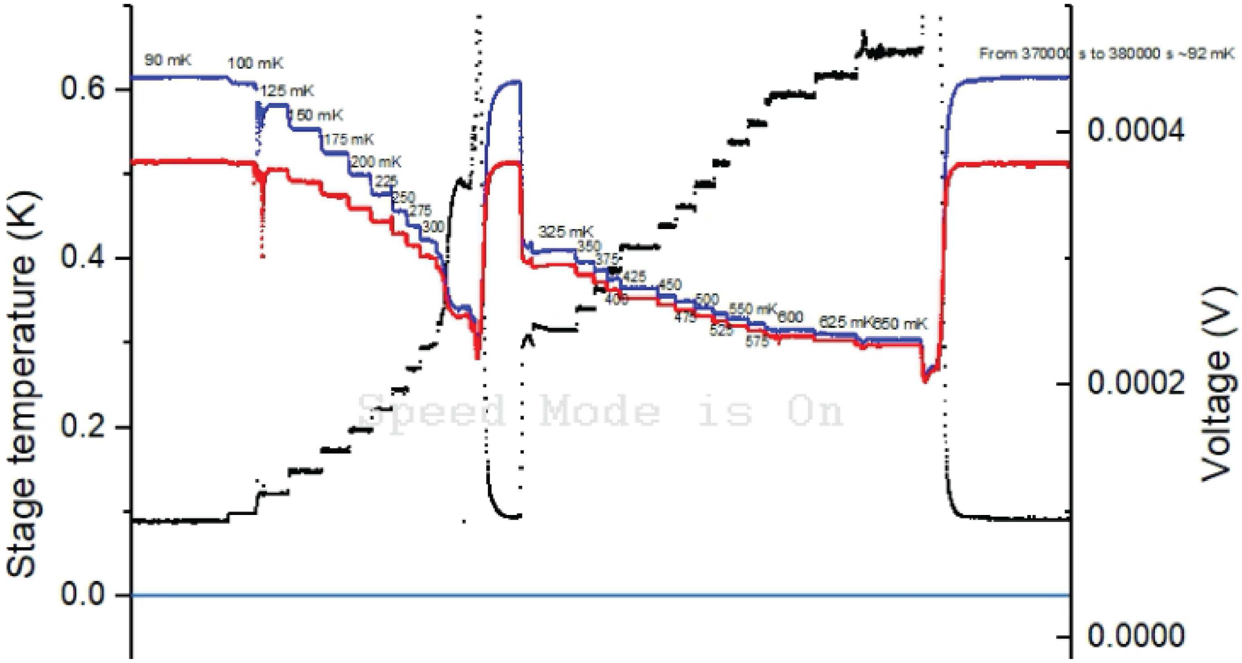

Figure 3.3. Display of the calibration process. The black points represent the temperature readings of the stage thermometer, with its axis on the left side. The blue and the red points present the voltage measured by the “cold” and the “hot” thermometer respectively, with the axis on the right, where the “cold” thermometer measures the colder side of the sample temperature gradient (further away from the sample heater). During the calibration process, only the stage temperature is altered through the stage heater, which by proximity, is very close to the temperature of the two thermometers. The temperature change causes the thermometer voltages to also change. The stage temperature is incremented up, and all the measurements at each step is averaged out. For each step, the stage temperature is mapped with the corresponding thermometer voltage, which is then used to interpolate the voltages of the two thermometers taken during the thermal transport measurement to acquire a temperature reading.

The power applied to the sample from the heater is calculated by using the relation $P = V^2/R$, where V is the voltage of the heater and R is the resistance of the heater. With the thermal gradient and the power of the heater, the thermal conductivity κ can be acquired, which is then plotted as κ versus T, where T is the average temperature between the two thermometers.

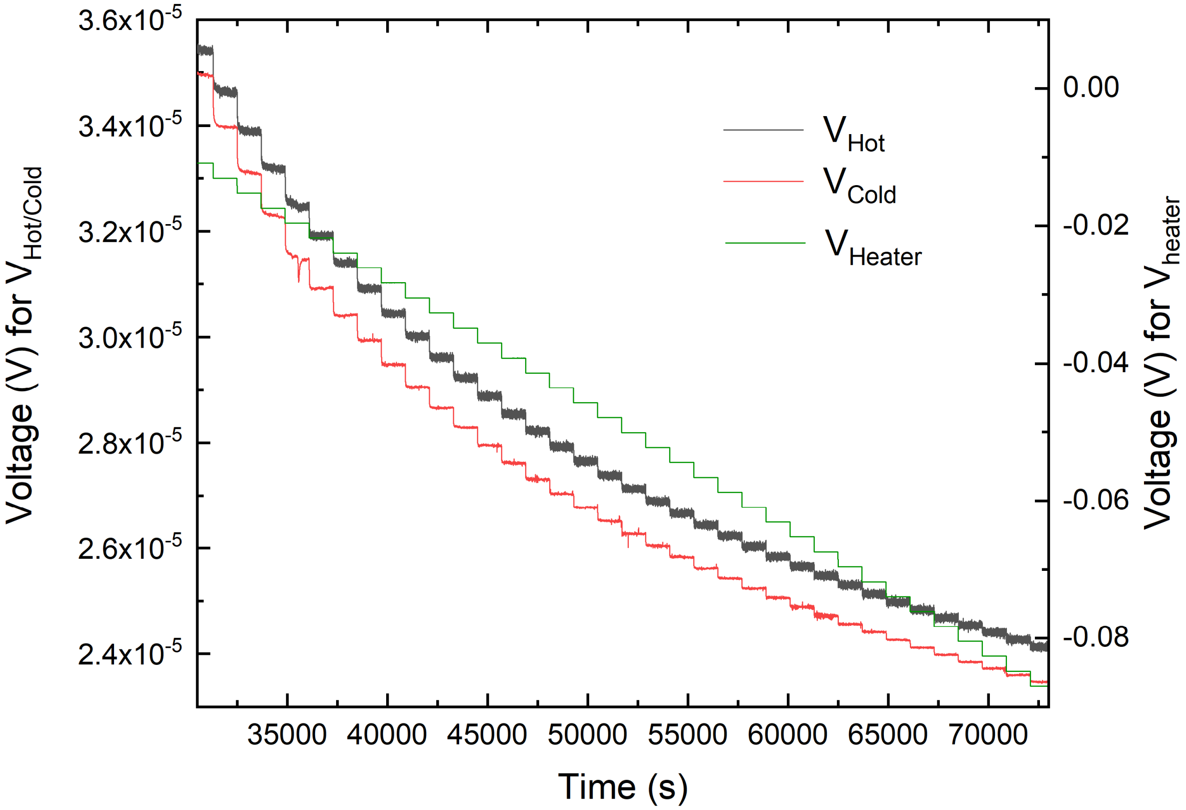

Figure 3.4 Data for the thermal conductivity measurement. V_{cold} and V_{hot} are the voltages of the thermometers measuring the colder or the hotter side of the sample (which is correlated with the side of the sample that is closer or further away from the sample heater). V_{heater} is the applied voltage of the sample heater. During the thermal transport measurement, the sample heater applies heat to the sample via using a high precision current source, and the thermometers measure the temperature gradient of the sample as voltages. These voltages are converted into temperature readings by interpolating the calibration measurement.

Chapter 4

Thermal conductivity of SmB_6 under uniaxial strain

4.1 Introduction

Electrical transport measurements on SmB_6 have shown gradual insulating behavior initiating at 40 K in the bulk associated with the opening of the Kondo gap [18]. A resistivity plateau appears below 5K due to the conducting surface, suggesting a topological nature of SmB_6 [19,34]. Various other studies have also supported the existence of topologically protected surface states; however, there are ambiguities regarding the nature of the bulk [15–17,20–23]. Recent studies of the de Haas-van Alphen (dHvA) oscillations in SmB_6 yielded contrasting conclusions about the Fermi surface, supporting both a 2D Fermi surface associated with the metallic surface states and an "unconventional" 3D Fermi surface with the insulating bulk [24,25]. Even though it has been shown that the emergence of dHvA oscillations is possible in certain band insulators like SmB_6, especially as a manifestation of the impurity moment-screening [56], the implication of a 3D Fermi surface could demonstrate the existence of charge neutral fermions in the bulk [25,30, 44]. A typical insulator behavior is explained as having a band gap, but if this is not the case, then this would open up the possibility of exotic insulators that goes beyond the Fermi liquid theory. This would mean that there could be interesting possibilities of these charge-neutral fermions coming as a formation of an exciton [45], a spinon from a fractionalized f-hole [46], or a Majorana fermion [30].

Thermal conductivity measurements allow the probing of bulk excitations that cannot be done with electrical transport measurements and can distinguish between fermionic or bosonic excitations. Compared to specific heat, thermal conductivity is immune from erroneous contributions from isolated embedded metallic impurities inside SmB_6 crystals unless the embedded impurity states percolate through the entire sample. Deviations from the thermal conductivity of a pure phonon gas would indicate charge neutral excitations. While the pure phonon gas contribution follows a cubic temperature dependence at low temperatures, the contributions from charge neutral fermionic excitations would emerge as a residual linear term in the $T = 0$ limit. Several thermal conductivity studies have been done on SmB_6 [28–30]. For flux-grown samples, there has been no observations of a residual linear term; however, there have been discrepancies between these studies regarding floating-zone grown SmB_6. The magnitude of the residual linear term between the studies either was in range with or violated the Wiedemann-Franz law, with the study that did observe a significant residual linear term concluding that it must be due to a charge-neutral fermion. Interestingly, similar phenomena of a residual linear term have been observed in floating-zone grown YbB_{12}, which is known to be another mixed-valent topological Kondo insulator [57]. The study also concluded that this must originate from a charge-neutral fermion.

Since the residual term has been observed in only floating-zone grown SmB_6, variations of sample growth may be a more crucial factor that must be considered. Flux-grown samples have been shown to contain pockets of aluminum that grow epitaxially to SmB_6 with similar structure and lattice constant, making it nearly impossible to identify from XRD [1,35]. However, floating-zone grown samples appear to suffer from non-stoichiometric crystal growth, which results in samarium vacancies of around 1% concentration due to the vaporization of samarium during the growth process [1,29]. These samarium vacancies are known to cause an enhancement of the Sm valence from the nonmagnetic Sm^{2+} to the J=5/2 magnetic Sm^{3+}[27,29] and thus may be responsible for the variance of thermal conductivity and dHvA studies between flux and floating-zone grown samples. Inverse-Corbino measurements have shown that Sm deficient samples appear to have a much higher bulk electrical conductivity, undercutting the expected nature of a highly insulating bulk [36]. High Hall mobility and low-temperature fermionic heat capacity were also observed for both stoichiometric and nonstoichiometric SmB6, suggesting a possibility of bulk conduction, though the samarium vacancies did not play a significant role for these measurements [47]. This residual bulk conduction was observed for floating-zone grown samples and had more dislocations that may originate from additional dislocations in the seed crystal used during sample growth [58].

As SmB_6 is a mixed-valence insulator, recent studies have attributed the valence fluctuations to the B_2 dimer having a temperature and pressure-dependent stretch and displacement that causes a change in the electron configuration and charge transfer, affecting the valence of the Sm ion [32,42]. This lattice distortion driven charge transfer mechanism suggests that the valence may be carefully tuned through applications of mechanical force. Previous work has demonstrated that uniaxial strain experiments are capable of tuning bulk energy scales, observable through the evolving bulk bandgap with tensile and compressive strain [33].

An application of controlled strain may be used as a tuning parameter to change the valence of the samarium ions, which, if the bulk is affected, may explain the mystery as to why there are contradictory conclusions to the current thermal conductivity studies on SmB_6. This method would be a “cleaner” way to study how deficiencies would possibly affect the bulk rather than doping studies, as possible introductions to dopants may compromise the changing vacancies as a dominant effect. We utilized a symmetrized design on the same uniaxial strain apparatus for our thermal conductivity measurements to simulate lattice distortion effects from Sm deficiencies present in floating-zone grown crystals, applying 0.27% uniaxial tensile strain to a flux-grown SmB_6. This will be used to investigate if there is a residual linear κ/T term without strain and observe if application of strain would affect the residual term by either causing an emergence or a significantly shift of the term.

It should be noted that the measurements shown on Figures 4.1, 4.9-4.11 were taken by Brian Casas, Figures 4.3, to 4.8 were taken by Laura Yu, and Figure 4.12 by both members.

4.2 Methods

SmB_6 crystals were grown in-house using the flux growth technique by Brian Casas. As shown in Figure 4.1(a), crystals with a needle-shaped morphology, with a cross-sectional area smaller than the overall length (L/A~10mm^{-1}), were chosen as potential candidates. Selected crystals were etched with 20% HCl solution for roughly 10 minutes to remove excess oxides and absorbed gases to ensure that contacts have low electrical contact resistance, which implies a good thermal contact between the crystal and the platinum thermal leads.

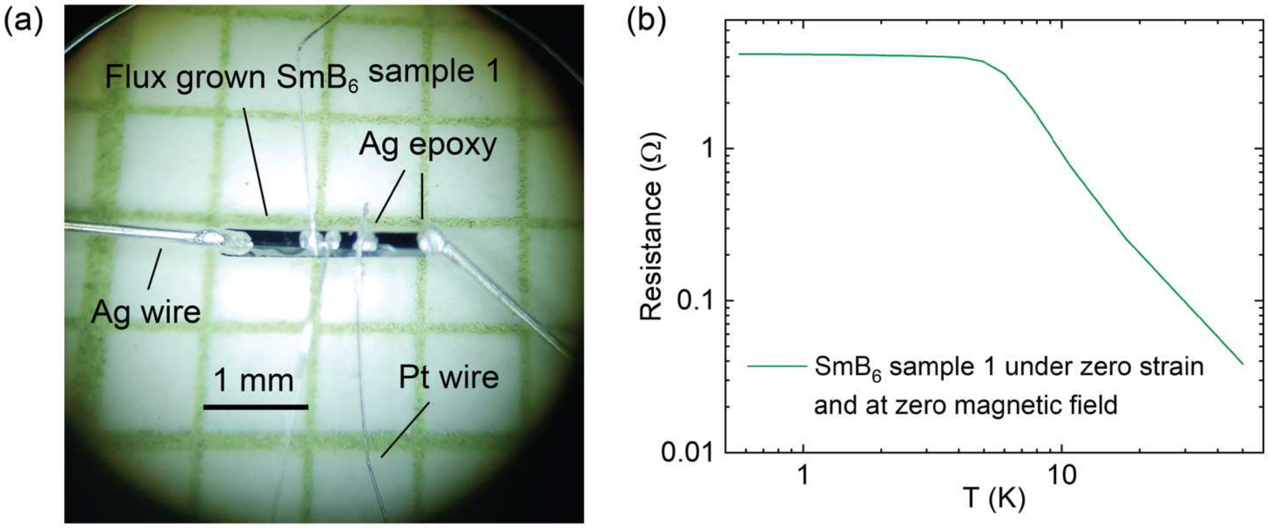

Figure 4.1. (a) A flux-grown SmB_6 crystal attached with silver and platinum wires using H20E silver epoxy for a thermal and electric transport measurements. The metal wires have been annealed on a hot plate to achieve better thermal conduction and mechanical flexibility. (b) Temperature dependence of the resistance for an unstrained SmB_6 crystal under zero magnetic field. The Kondo gap opens at ~34.7 K, while the resistance plateaus to 4Ω at ~3K. The emergence of a very low resistance saturation indicates high sample quality.

Platinum wires of 25 micron diameter are used to establish thermal contact between the crystal and the micro-sized RuO_2 film thermometers or the heater. These wires provide high electrical and thermal conductivity and the capability to decrease the contact size due to their size and flexibility, which are crucial as the strained portion of the crystal is only 1 mm. Thermal grounding is provided by 500 micron silver wires. All contacts are attached along the naturally grown <100> face via H20E silver epoxy and were cured at 80°C for three hours to ensure high mechanical stability. Both types of contacts do not seem to provide additional contact resistance. Typically in electric transport measurements, the electric contact resistances were ~1 kΩ, though for this thermal experiment minimizing the time between the etch and contact placement has resulted in contact resistances $< 100\ \Omega$, an improvement over contact resistances reported on SmB_6 [25,29]. Figure 4.1(a) shows a SmB_6 crystal with such contacts. A four-probe resistance measurement was performed by Brian Casas on a single SmB_6 crystal under zero magnetic field. As shown in Figure 4.1(b), thermally activated behaviors were observed at higher temperatures with a fitted bulk activation gap of 34.7 K that is consistent with previous reports. A resistance plateau of a very low saturation resistance of 4 Ohm occurs below 5 K, indicating high batch quality.

Conventional steady-state thermal transport technique is analogous to a four-probe electrical resistance measurement, where current is injected and drained to electrical ground by two outer contacts while the two inner contacts are used to measure the voltage drop. For thermal conductivity measurements, the two outer contacts would inject and drain the heat current to the thermal ground, and the two inner contacts would measure the thermal gradient across the sample. These conventional thermal transport experiments would typically require the sample to be suspended in vacuum to minimize the heat loss to the surrounding environment. However, applying a substantial amount of strain measurements to a SmB_6 crystal requires strong mechanical coupling of each end of the sample to the uniaxial strain cell [33]

. The strong mechanical clamping unfortunately leads to a high degree of thermal contact to between both ends of the sample and the strain cell. Therefore, a new thermal conductivity measurement design is needed to work with the strain apparatus. To resolve this issue, we have invented a symmetric thermal conductivity design by symmetrically mirroring the geometry of the conventional thermal conductivity setup was modified to reflect it across the suspended end such that the heater is relocated to the center of the sample while both mechanically clamped ends serve as thermal grounds, as shown in Figure 4.2(a). Heat current is injected by the sample heater at the center of the sample, with the heat current splitting off at the right and the left side of the heater. The two thermometers are mounted between the heater and a single thermally grounded end. This setup allows both ends of the crystal to be thermally grounded by the same silver wires, which would be thermally coupled to the sample stage. If the heater is placed at the center of the crystal, the temperature gradient across the crystal should be maximized at the center of the crystal and symmetrically decrease closer to the thermal ground. To account for the deviation of the heater's position from the crystal's center, the expression for thermal conductivity κ(T) is

$$\kappa = \frac{P}{\Delta T}\frac{l_R}{(l_L+l_R)}\frac{L}{A} \tag{1}$$

where P is the power dissipated across the heater, ΔT is the thermal gradient, l_L is the distance from the heater to the left thermal ground in Figure 4.2(a), l_R is the distance from the heater to the right thermal ground, L is the separation between the two thermometers, and A is the cross-sectional area of the crystal. Apart from the heater placement, Equation (1) implies perfect symmetry in other aspects of the experimental setup. A practical complication with utilizing this symmetric thermal transport design arises from asymmetries in the experimental design, contact resistances, and epoxy thickness. These factors make it so that it is not possible to know the precise applied heat current passing through the probed section of the sample, which can lead to errors in the absolute value of the measured thermal conductivity. We note that the temperature dependence, which is the main subject of this paper, should remain accurate even in the presence of significant asymmetry. Nevertheless, for measurements aiming at high absolute precisions, a more precise model for the experimental geometry can be made through an equivalent circuit as shown in Figure 4.2(b), where the resistances of various sections of the crystal and the contacts are all assumed to have a unique value while resistivity is considered to be consistent along the length of the crystal. In this model, the thermometers are located on the right side of the heater. The resistances R_{LC} and R_{RC} are of the contacts and the H20E silver epoxy on the left and the right side of the heater, R_L is the sample resistance on the left side of the heater, R_S is the section of the crystal measured between the two thermometers, and $R_{S'}$ is the unmeasured section of the crystal. With these considerations, the thermal conductivity is

$$\kappa = \frac{2P\,\frac{1}{A^2}l_s l_L}{-x \pm \sqrt[2]{\left(x^2 - 4\left(P\frac{l_R l_L}{A^2}\right)(-R_{RC}\Delta T)\right)}} \tag{2}$$

where $x = R_{LC} P \frac{l_S}{A} - \Delta T \frac{(l_R + l_L)}{A}$.

In our experiments, the data suggests that utilizing Equation (1) alone would yield sufficiently accurate results, as compared to the values measured with the traditional thermal setup. This indicates that when the sample and the experimental setups were made sufficiently symmetric, as it is in our case, the difference between Equation (1) and Equation (2) is not significant. For this reason, we use Equation (1) throughout this chapter.

The strain part of the experiment setup is based on the recent development in a strain apparatus adopting a tri-piezo technique ensures a controllable application of tensile strain between -0.5% to 1%, with more than 70% of the strain transferring from the piezo to the sample [33]. The very same device is used in this paper to apply up to 0.27% uniaxial strain of a flux grown SmB_6 with dimensions $2.85 \times 0.635 \times 0.558$ mm^3. The strain apparatus and the associated thermal transport components were installed onto a home-built dilution fridge sample stage made of Teflon and gold-plated annealed silver wires, plates and posts to minimize eddy current heating at mK temperatures. The SmB_6 sample is prepared with the contacts in configuration for the symmetric setup [Figure 4.2(a)]. The ends of the crystal are clamped and thermally anchored to strain apparatus and the dilution refrigerator stage as shown in Figure 4.2(c), mounted using Stycast 2850FT epoxy and catalyst 24 LV, which is then cured at room temperature for at least 24 hours. The symmetrized thermal transport geometry is partially obscured by the black Stycast 2850 epoxy mounting the crystal to the steel washers. The three contacts on the sample shown in the zoomed-in portion of Figure 4.2(c) are located in the center of a gap approximately 1mm in size.

Thermal grounding to the crystal is established through silver wires indium soldered to a silver foil that has been screwed onto the sample stage, which allows a high degree of thermal contact to the mixing chamber. Electrical leads for the heater and thermometers are made using coiled manganin wires, which are shown to be highly thermally insulating within the temperature range of interest. The addition of the Stycast 2850 epoxy for sample mounting likely accounts for some small additional thermal grounding, though it is weakly coupled to the stage through the stainless steel washers and the titanium strain cell frame. The amount of applied strain was determined by utilizing the calibration from the previous strain gauge measurements since the same strain apparatus was used with an unchanged strain gauge and gap size. Thermal conductivity measurements were taken under the Quantum Design He3 PPMS for temperatures above 400 mK and a Kelvinox-MX 250 dilution refrigerator in the sub-Kelvin temperature range.

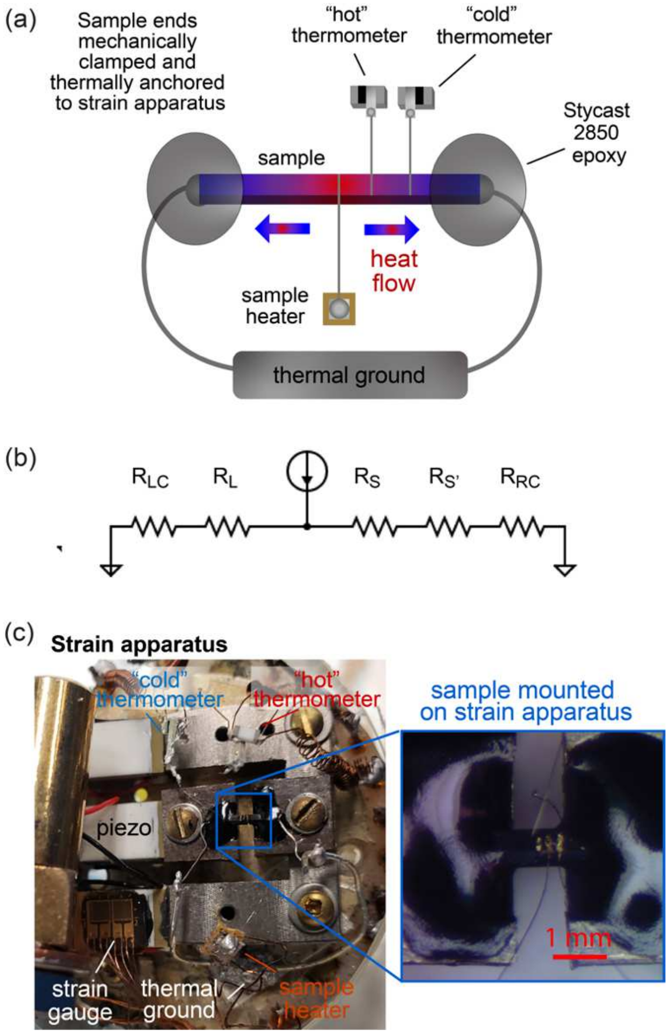

Figure 4.2. (a) Symmetrized thermal conductivity design. The sample is mechanically clamped and thermally anchored to the strain apparatus. This is done by the silver wires epoxied to the ends of the crystal that lead to the thermal ground and Stycast 2850FT epoxy that secures the crystal to the titanium washers. The thermometers measure the thermal gradient from the heater to one end of the sample. (b) Equivalent circuit model for the symmetrized design. The heat current splits to the heater's left and right side and drains at the thermal ground. R_{LC} and R_{RC} are the contact resistances, R_L is the sample resistance on the left side of the heater, R_S is the resistance of the probed section of the crystal, and $R_{S'}$ is the resistance of the unmeasured section of the crystal. (c) Symmetrized thermal conductivity design on the strain apparatus. Thermal grounding is provided by the silver wires from the ends of the crystal that are indium soldered to a silver foil screwed onto the stage. The zoomed-in image shows the mounted SmB_6 and the contacts within the 1mm gap that will be strained.

4.3 Unsuccessful Attempts

Some unsuccessful attempts for the measurements have been due to primarily having improper contacts of the stage components (for example, the silver foil used for soldering silver wire to the sample not making proper contact to the thermometer), large thermometer noise, and the electrical grounding issues originating from both the wiring of the measurement equipment and the unstable grounding provided by the building. Improper contacts can generally be found quickly, as they can be found either before the experiment or during the room temperature measurement. Before the experiment, there may be shorting when attempting to measure the resistance through the stage components since the resistances of the thermometers and the sample heater are known. A more common occurrence is the platinum wire coming off the sample while setting the stage to the dilution fridge since the platinum wire is 25 microns in diameter and the stage is implemented upside down, which could pull down the wire off the sample. The wires that come off the sample cannot be verified electrically since the sample and the platinum wires are too small. Any attempts at trying to measure through additional stage components (such as through the silver foil or the thermometer) to verify the platinum wire connections to the sample will be dominated by the resistances of these components. Therefore, the platinum wires connected to the sample and the silver foil must be verified visually. Additionally, during the room temperature measurement, there may be no voltage readings through the thermometers due to disconnections in either the thermometer to the stage or the stage to the breakout box. The thermometer is electrically connected to the stage through the manganin wire, so the disconnections on the thermometer to the stage can be found by making sure the manganin wire connections are properly made. However, any issues regarding the connection to the stage to the breakout box may not be as straightforward, since this could include issues in the dilution fridge connection which may not be fully accessible. The typical disconnections mostly occurred on the accessible points of the dilution fridge where there are exposed copper wires connecting the stage to the dilution fridge. If the setup process of the stage to the dilution fridge was handled too roughly, these copper wires can be split off, which would require the ends to be soldered back together.

The noise from the voltage measurements of the thermometer may be large enough so that the voltage steps may be obscured while incrementing the heater. This is due to the inadequate amount of thermal cycling via liquid nitrogen on the thermometers, as the internal stresses within the alumina substrate of the thermometers must be sufficiently relieved. This can be seen in Figure 4.3, where the thermometer measuring the colder end of the sample has a larger noise than the thermometer measuring the hotter end. Experimentally, we have found that a sufficient number of cycles is ~40 cycles. The thermometers would be additionally cycled a few times on the PPMS to verify if the cycled amount was sufficient and to provide further cycling. Figure 4.4 shows a thermometer undergoing the cycling process on the PPMS, with the overlapped sweeps implying that there was ample liquid nitrogen cycling on the thermometer.

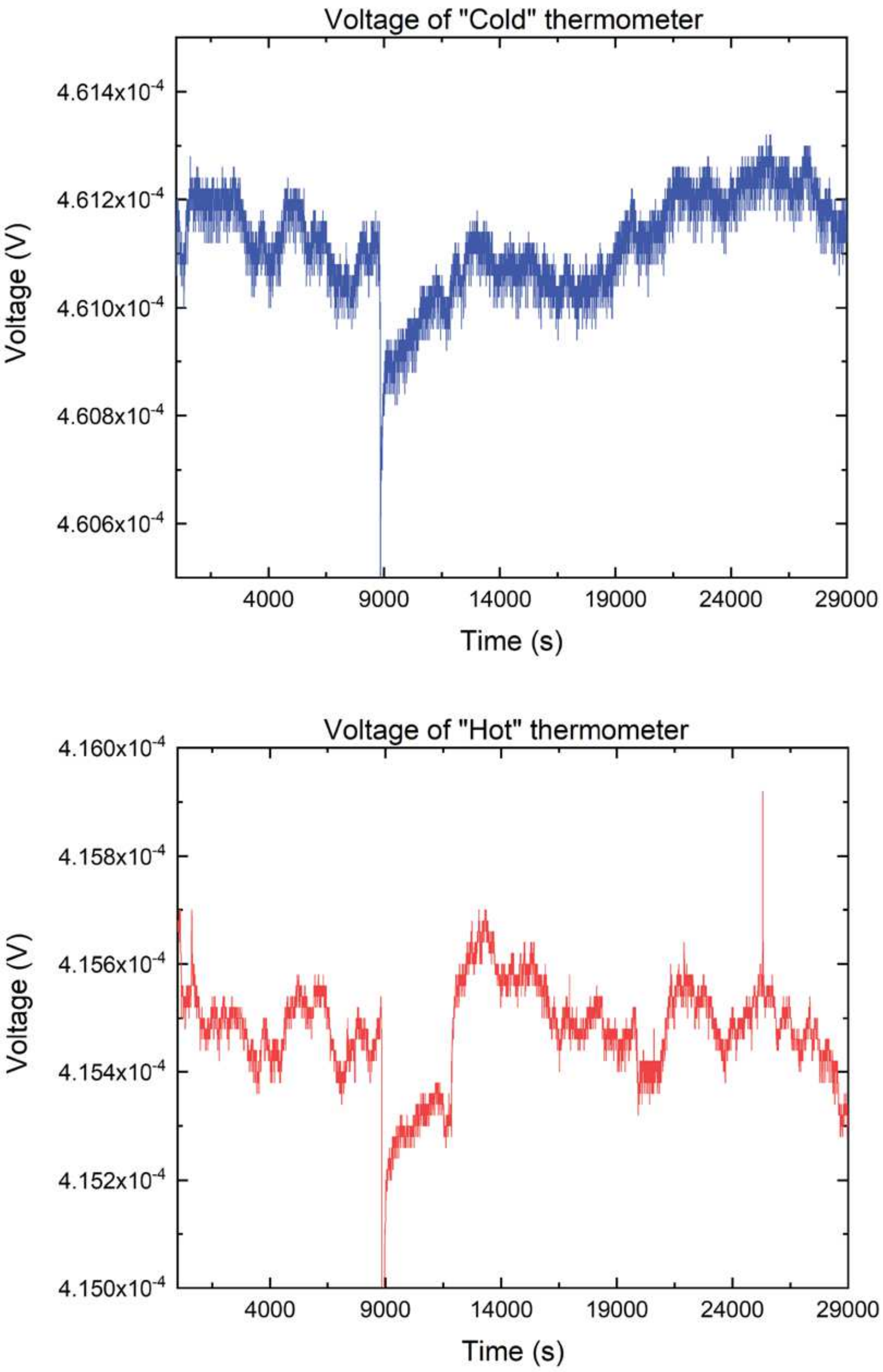

Figure 4.3 Voltage measurements of the sample thermometers, with “cold” and “hot referring to the thermometer measuring the colder or hotter end of the sample. The “cold” thermometer underwent smaller amount of cycles than the “hot” thermometer, which consequently has a larger noise than the “hot” thermometer.

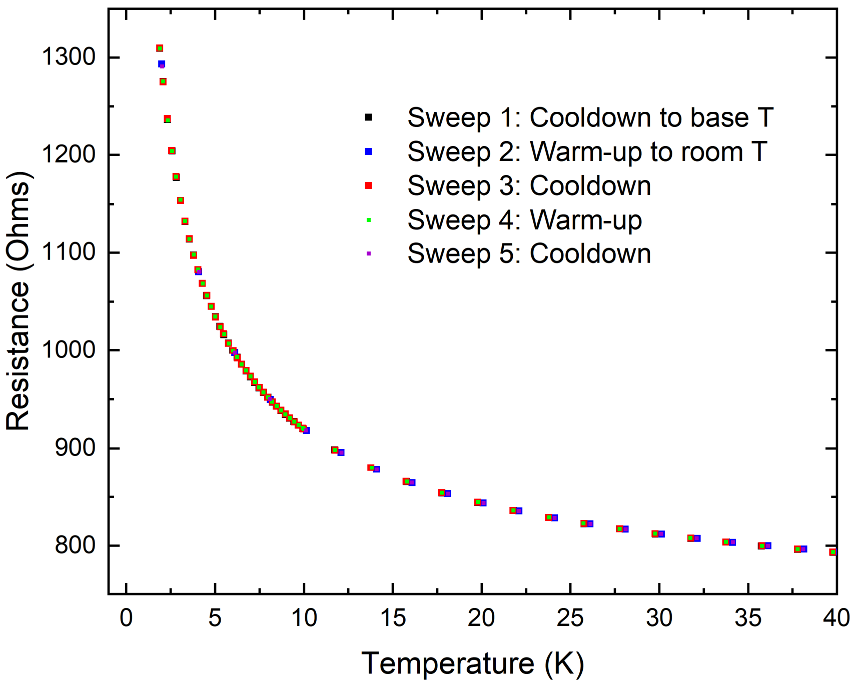

Figure 4.4 Thermal cycling of a thermometer on the PPMS. This is done to verify if the thermal cycling via liquid nitrogen was sufficient enough as well as provide further cycling on the thermometer. The overlapped resistance of the thermometers indicates that the thermometer has undergone enough liquid nitrogen thermal cycling.

Grounding issues are harder to identify, as they are generally detected during the measurement and may not have a direct resolution. So far we have detected two types of grounding issues that have compromised some of the measurements. The first type of grounding issue was due to the inconsistent grounding between the measurement equipment, as the outlets located on the top and bottom of our rack that is used to connect all the measurement equipment had a slightly different ground. Accounting for the ground of the rack connections along with providing proper electrical shielding and wrapping the pairs of coaxial cables together into a twisted pair which helped reduce the electrical fluctuations and noise of the experiments. The consequence for this improper grounding can be seen by the thermal conductivity measurement of SmB_6 under 0.27% uniaxial tensile strain in Figure 4.5, where there is a linear trend in κ/T only within a small region before undergoing fluctuation.

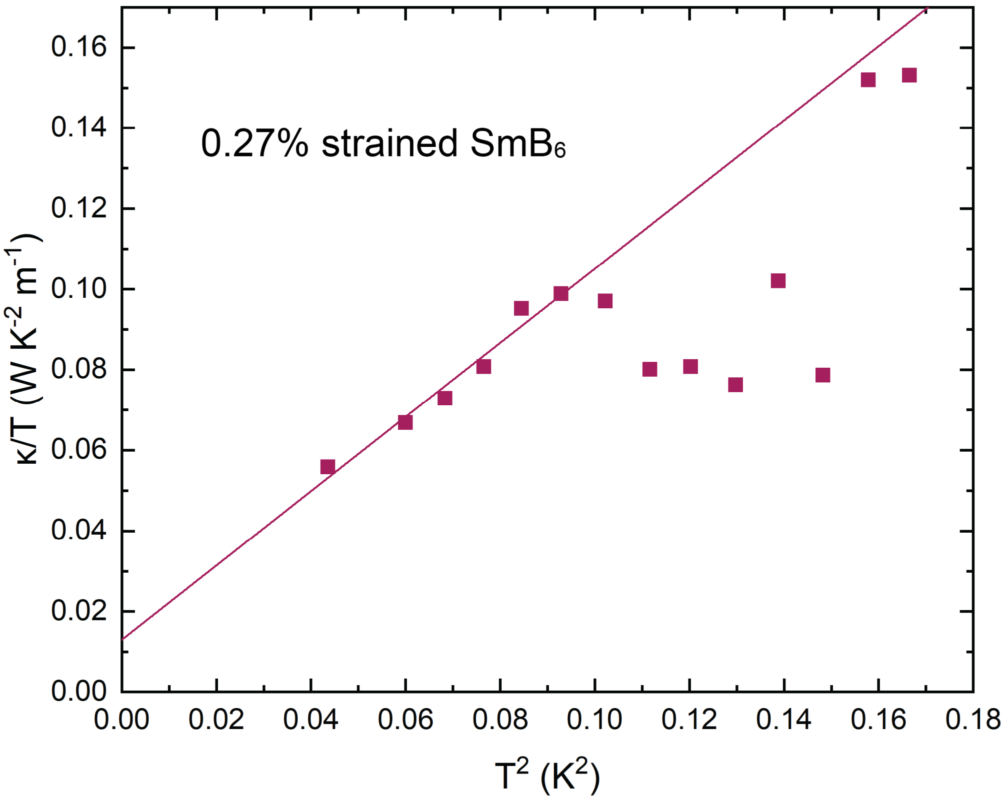

Figure 4.5. Thermal conductivity measurement with improper grounding on a SmB_6 crystal under 0.27% uniaxial strain (sample 3). Due to the grounding not being properly considered, the expected linear behavior of κ/T is only observed up to some partial range until fluctuations occur.

The second type of grounding issue was discovered as a periodic behavior of the voltage measurements on the order of half a day, as shown by the voltage measured through both thermometers as shown in Figure 4.6, and cannot be resolved through the laboratory due to this issue originating from the building ground. This means that the calibration and the thermal transport measurements must be completed within half a day while there is minimal periodic voltage background. In Figure 4.7, the number of steps for both the calibration and thermal transport measurements was doubled, well-surpassing the time span that has the acceptable electronic fluctuations. This is evident by the gaps in the measurement, where the fluctuations originating from the building caused non-uniform steps coupled with even more fluctuations from the longer measurements affecting both the calibration and the thermal transport. Figure 4.8 shows the overlapped data for the thermometer voltages and κ/T, showing the approximate occurance of the gaps with the instable voltages. Thus it is critical to take account of electrical grounding issues for a highly sensitive electrical measurement, as each thermal transport step size can be as low as 1mV, so the electrical noise must be much lower than this value.

Generally, electrical issues from the setup can be found before the cooldown occurs, as most issues are primarily due to shorting or accidental removal of contacts. However, thermal contraction may also cause these issues even when the room temperature measurements were done successfully. Therefore it is crucial to take test measurements under each stage of the cooldown before moving forward to the actual experiment, as trying to repair electrical connections to the stage would require the initiation of a time-consuming sample change procedure.

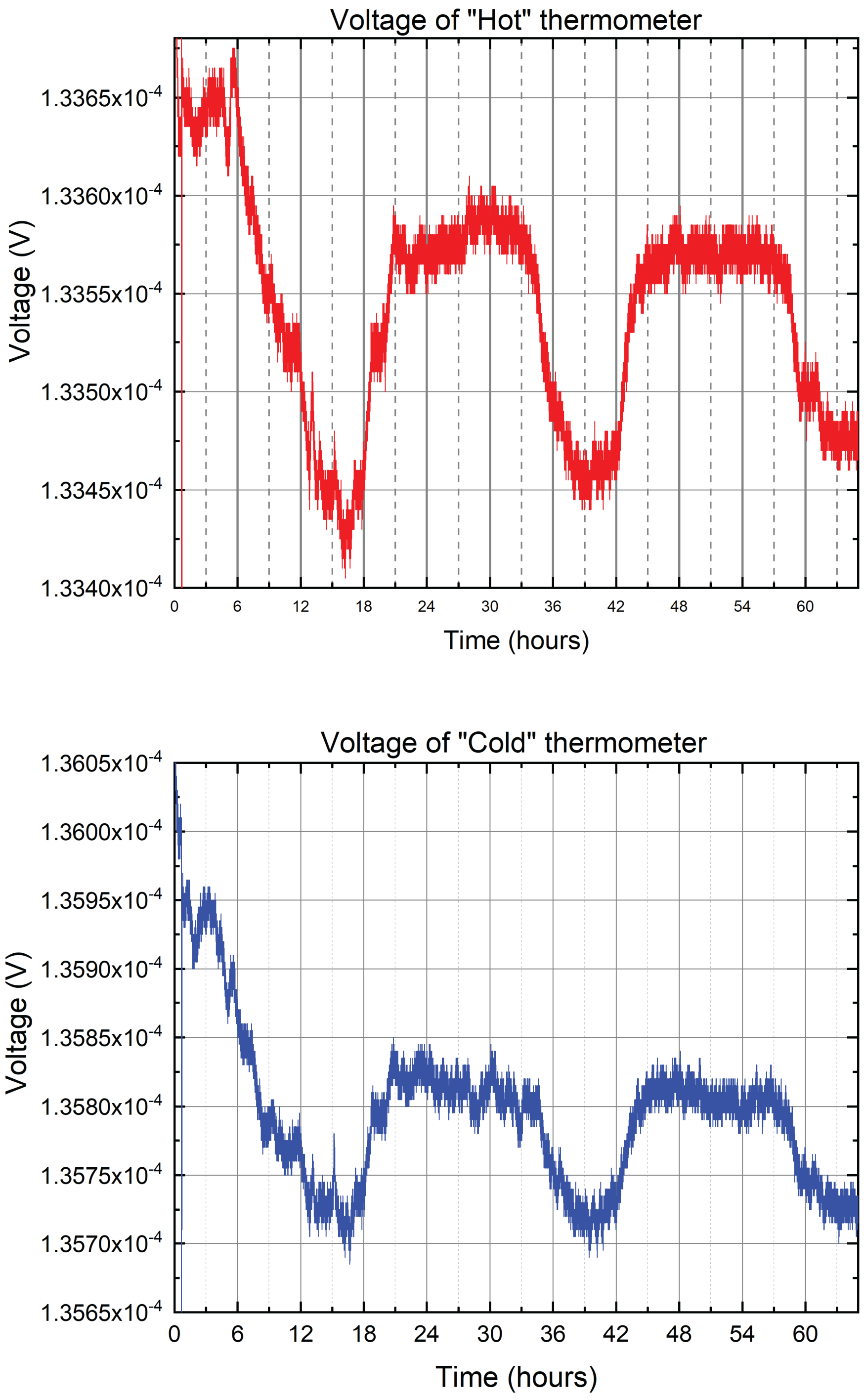

Figure 4.6. The voltage measurement of both thermometers connecting to the sample. There was no application of heat from either the still heater or the stage heater. The periodic behavior spanning a couple of hours originates from the unstable grounding provided by the building. In order to get around this, measurements are taken at a certain time of the day and completed within a few hours.

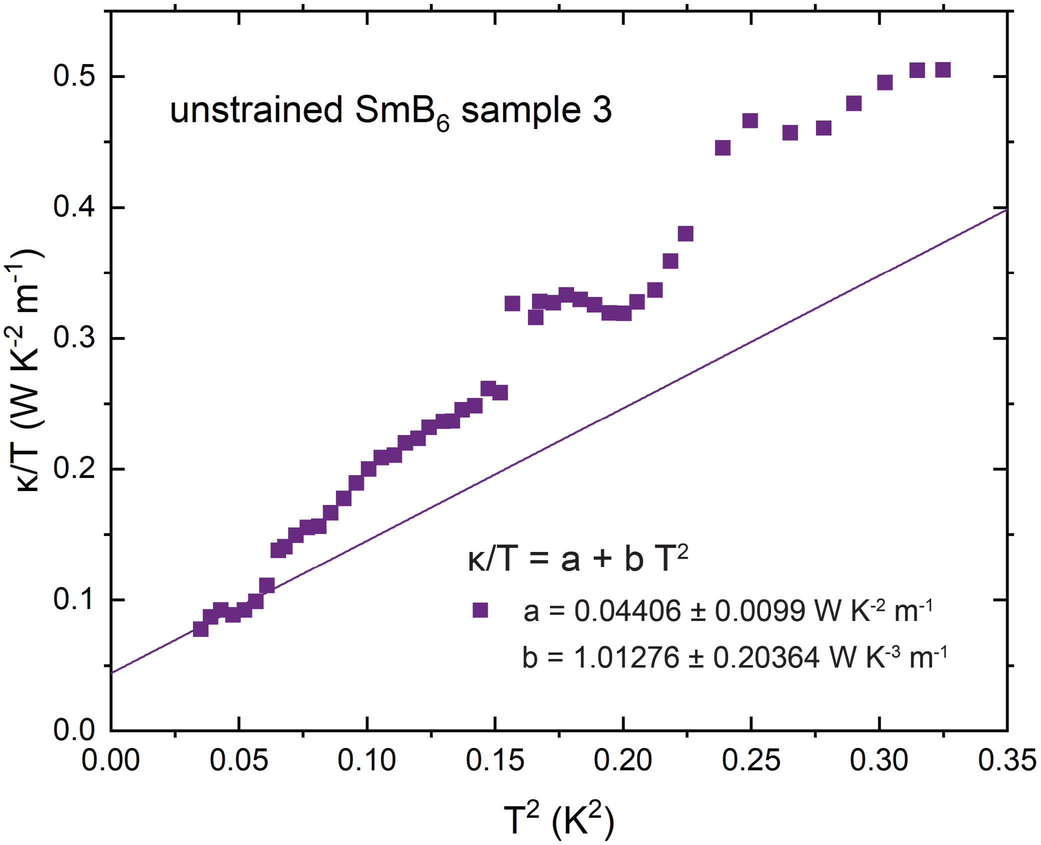

Figure 4.7. Thermal conductivity of an unstrained SmB$_6$ crystal measured under unstable building ground. The number of steps for both the calibration and the thermal transport was doubled, surpassing the time slot for when the grounding from the building was stable. This caused the steps from both the calibration and the thermal transport to become non-uniform, causing gaps in the **κ**/T measurement.

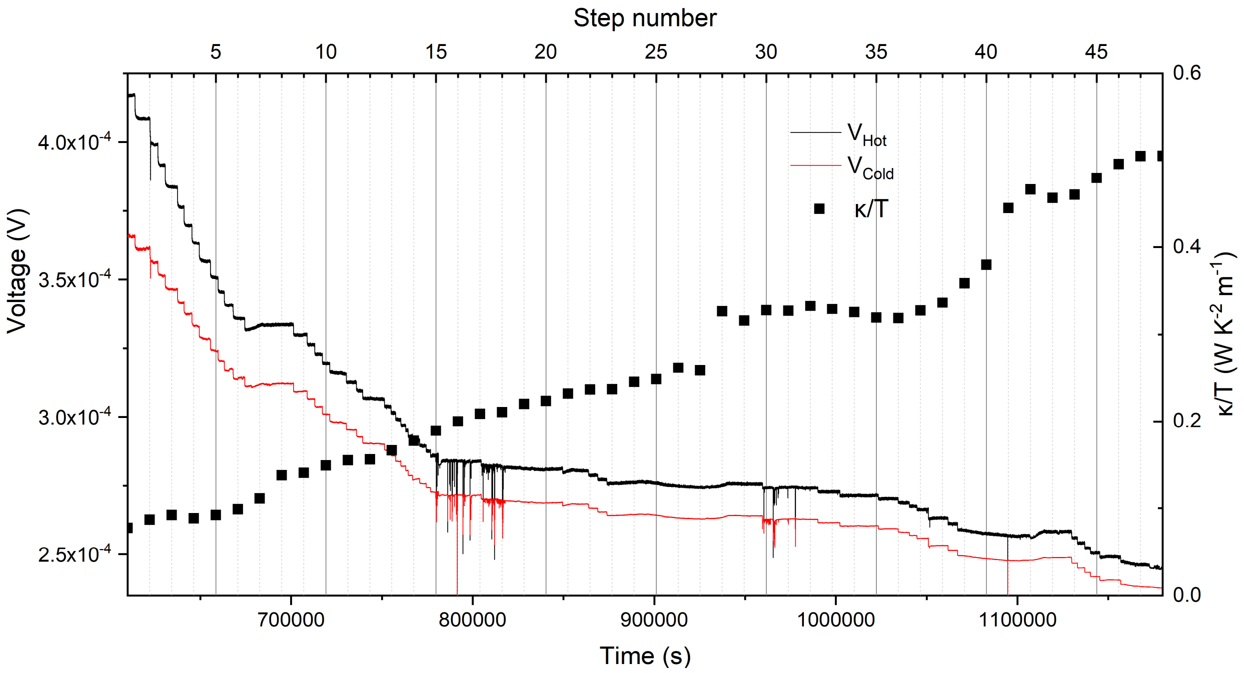

Figure 4.8 Thermometer voltages plotted voltage versus time and κ/T from Figure 4.7 versus averaged step number. The data for κ/T are taken from the time averaged steps of the thermometer voltage. Since the voltage steps are not uniform, the κ/T data points do not perfectly align with the steps; however, the approximate occurance of the gaps in κ/T can be closely correlated with the voltage instabilities.

4.4 Results

4.4.1 Sample Quality

First, to confirm the quality of the samples from this batch of in-house grown crystals and to verify the accuracy of our new symmetric thermal setups against the traditional method, Brian Casas performed thermal conductivity measurements with the traditional four-probe steady-state method on the PPMS. In the higher temperature range, there is a visible peak in the thermal conductivity at ~9K as shown in Figure 4.9, indicative of a transition between electron-phonon scattering and multi-phonon scattering channels. The peak height signifies high sample quality, as it is nearly 20% higher than data presented in the literature [42].

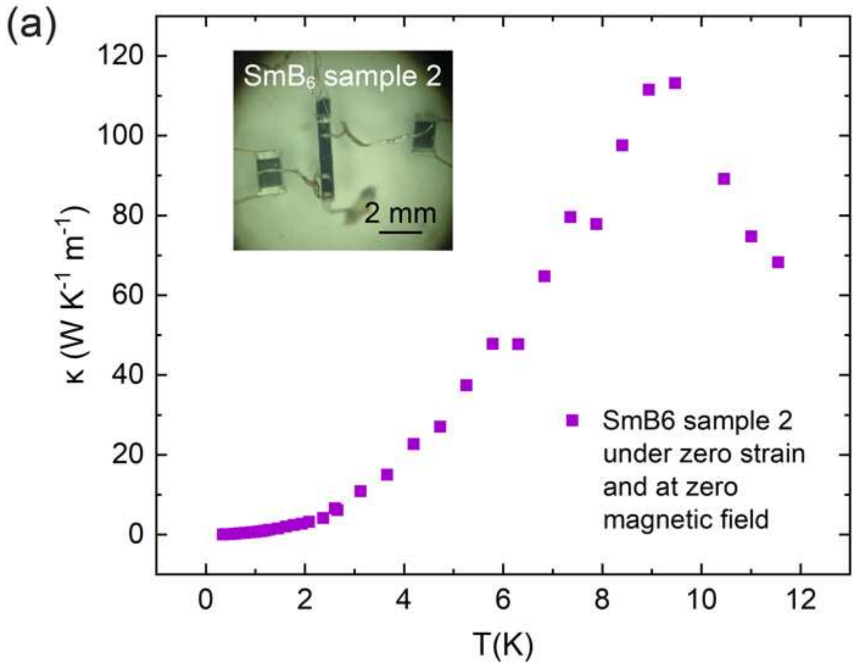

Figure 4.9 Thermal conductivity of SmB_6 from 0.4K to 12K. The peak at ~9K indicates high sample quality and is a key feature in insulating crystals. The inset shows the prepared SmB_6 crystal used in this measurement.

Thermal conductivity was measured from 0 T to 9 T by Brian Casas on the PPMS, as shown in Figure 4.10. The field dependence appears smaller than in previous work, though estimates suggested this is due to J = 5/2 moment likely caused by the Sm^{3+} ions. The close agreement of the data below 700 mK with known phonon conductivity indicates that there is only evidence for a bosonic heat carrier at these temperatures. Previous reports [30] show that even above 400mK, signatures of a fermionic excitation could be observed under an applied field, though measurements starting at 100mK would be stronger evidence for possible fermionic excitations.

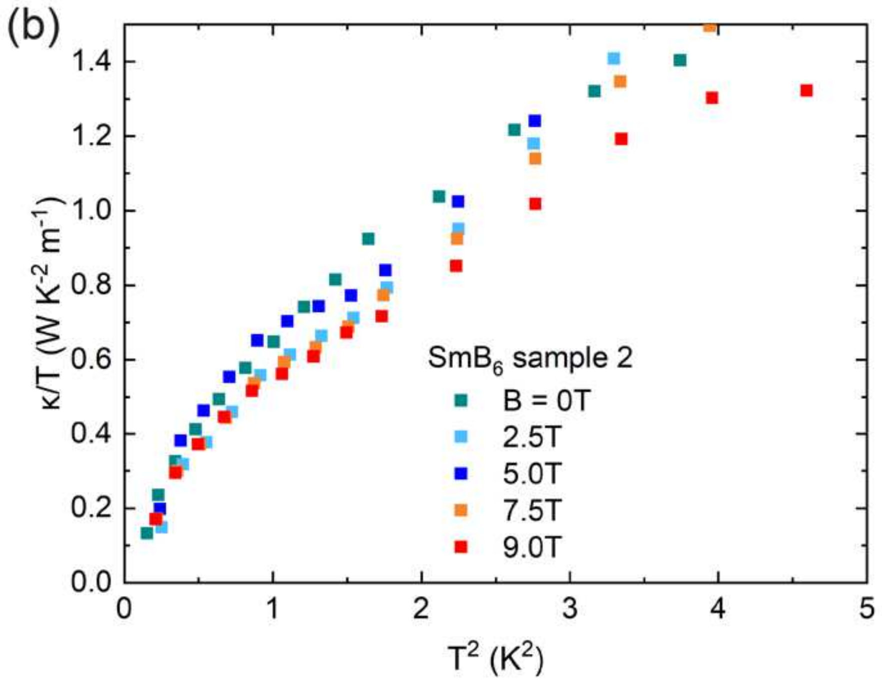

Figure 4.10 Thermal conductivity of SmB_6 as a function κ/T versus T^2 below 5K. Data shows a non-monotonic field dependence, suggesting a field-induced phonon scattering suppression. The figure shows the magnetic field and temperature dependence of the thermal conductivity. There is a non-monotonic behavior induced by the magnetic field, with previous reports attributing this to a Schottky type anomaly for phonon scattering from magnetic moments.

4.4.2 Conventional Versus Symmetric Design

Typical thermal transport measurement is done on a “conventional” 4-probe setup, where the ends of the crystal are connected to the heater and the thermal ground and the thermometers along the length of the sample. However, trying to implement this setup on the strain apparatus would cause a heat leak on both ends of the crystal, so our group developed a symmetrized thermal transport design. To verify if the symmetrized design would not significantly affect the thermal conductivity measurements compared to that of a typical, or “conventional,” setup, Brain Casas measured both designs on the PPMS. By comparing measured thermal conductivity using both methods on a single crystal [Figure 4.11], it was verified that the new symmetrized thermal conductivity design indeed yields accurate quantitative values of κ(T) compared to the conventional 4-probe thermal conductivity setup. A single SmB_6 crystal was prepared with three platinum wires for the heater and thermometer contacts and two silver wires for the thermal ground. This sample was first measured in the "conventional" geometry, where heat is applied through one end while the other end is thermally anchored. As such, the wire for the heater in the symmetric geometry is left floating in the conventional measurement. In the symmetric thermal measurement, the sample is mounted on the strain apparatus but with zero piezo voltage, yielding essentially no strain in the sample. A small amount of strain could rise due to the differential thermal expansion, but is minimized due to the tri-piezo geometry of the strain apparatus.

The measurements were done with no magnetic field and then at 5T, as shown in Figure 4.11. The data displays no appreciative difference in the thermal conductivity between the symmetric and the conventional setup with no field [Figure 4.11(a)] and with 5T [Figure 4.11(b)]. The data for both conventional and symmetrized design is within range with the other thermal conductivity measurements done on SmB_6 [28-30].

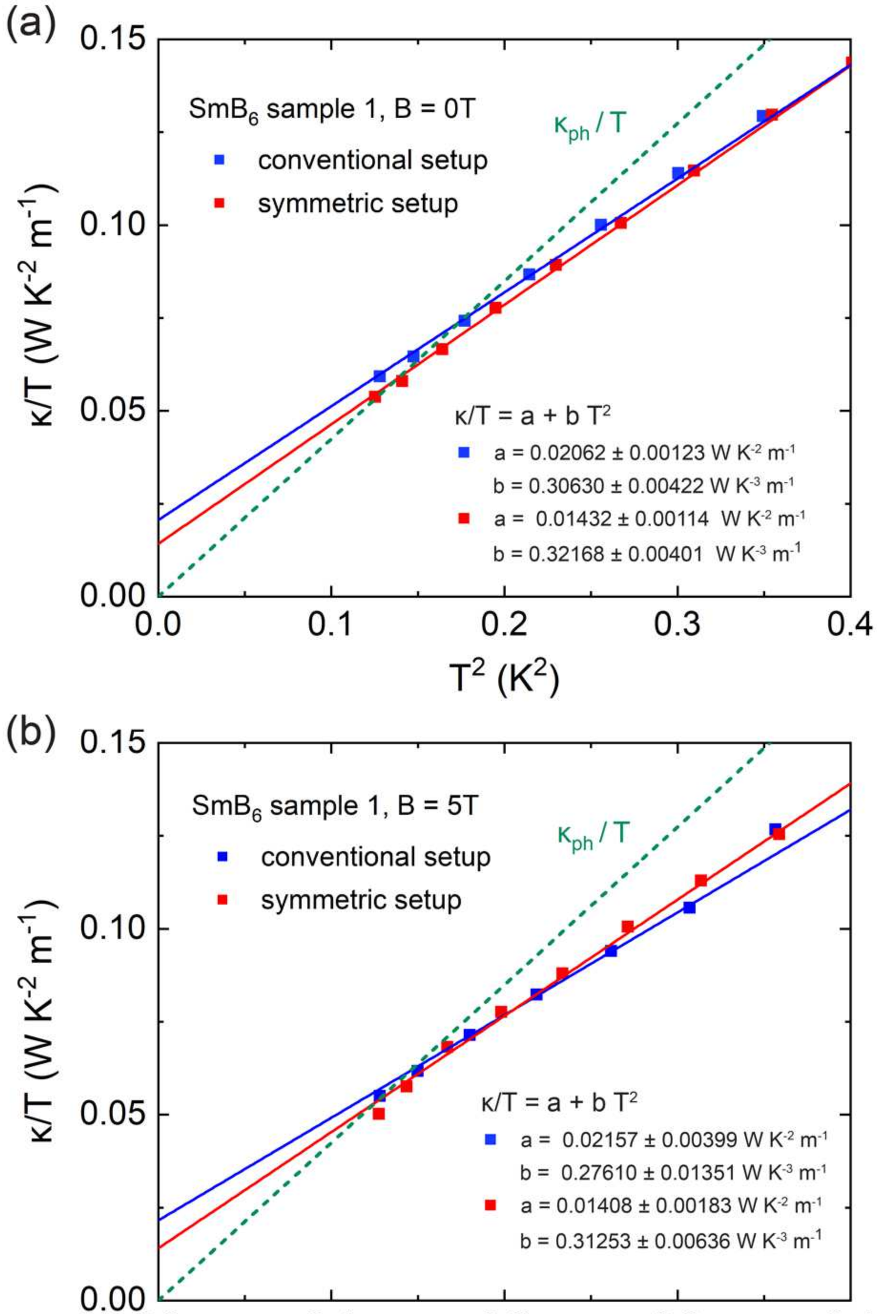

Figure 4.11. Thermal conductivity as a function of κ/T versus T^2 of SmB$_6$ for conventional and symmetric setup (a) under no field and (b) under 5T. The dashed lines show linear fits below ~0.6K. A SmB$_6$ crystal was prepared with the symmetric setup, but for the conventional measurement, heat current was applied on one end of the crystal. No significant difference in κ(T) was observed between the two different setups.

4.4.3 SmB_6 under strain

Finally, we have performed measurements with strains applied to the sample. The thermal conductivity of flux-grown SmB_6 under no strain and under 0.27% uniaxial tensile strain is plotted as κ/T versus T^2 as shown in Figure 4.12, with the solid lines being the linear extrapolation of the data. In the limit of $T \rightarrow 0K$, the phonon conduction κ_p/T is proportional to T^2, so the residual linear term was extrapolated from κ/T versus T^2 to determine if there were fermionic heat carriers. The metallic surface state would yield a negligible contribution of the thermal conductivity, as estimations using Wiedemann-Franz Law $\kappa/T = L_0/\rho$, with L_0 the Lorentz number would yield the highest contribution of κ/T in order of 10^{-6} mW K^{-1} cm^{-1}. The acquired linear terms for both unstrained and strained measurements were on the order of 10^{-1} mW K^{-2} cm^{-1}.

The slope, or the phonon contribution from T^3 term, did change with the strain as expected, due to the changing lattice constant of the crystal. Another possible contribution to the changed slope of κ/T may be due to the changes in the impurity scattering of the phonons. So far, attempts to apply compressive strain have not been successful due to the thermometer detaching from the crystal. A possible solution to this may be to change the H20E silver epoxy connecting the platinum wire to the sample to spot-welding the platinum wires.

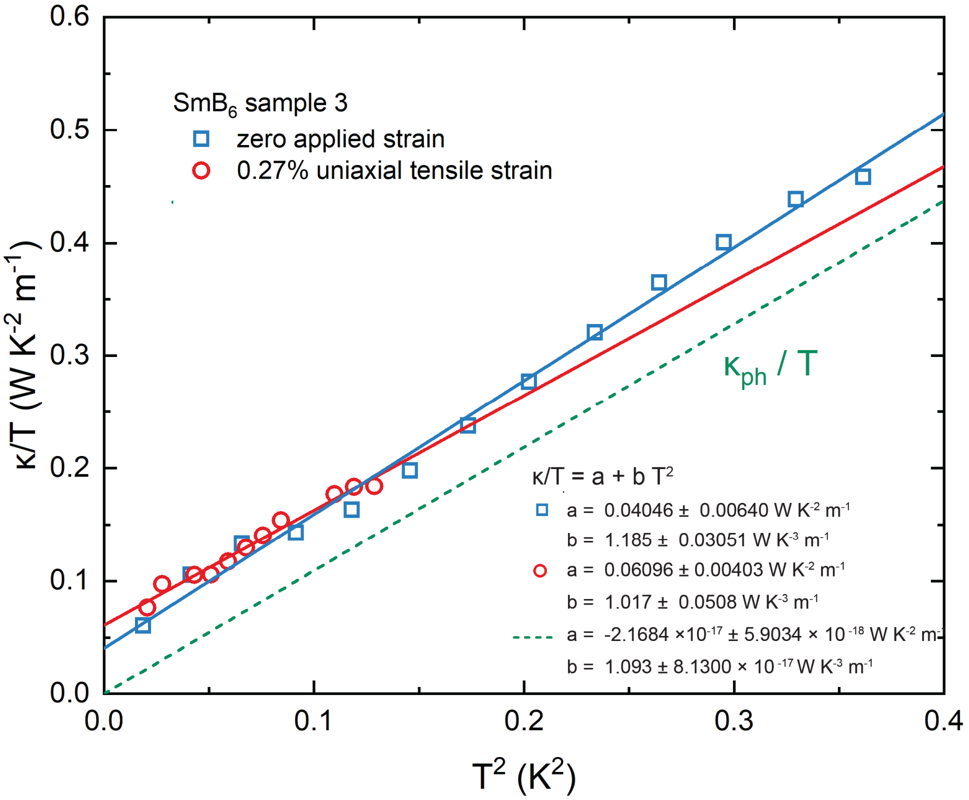

Figure 4.12. Thermal conductivity of a single flux-grown SmB$_6$ as a function of κ/T versus T for no applied strain and under 0.27% uniaxial tensile strain. Residual linear term for κ/T was extrapolated via a linear fit of T^2, which yields values in the order of 10^{-1} mW K^{-2} cm^{-1} for both unstrained and strained SmB$_6$.

4.5 Discussion

Previous pressure and strain studies for SmB$_6$ have demonstrated that the bulk and the surface change dramatically with changes in pressure or the application of mechanical strain [33, 43]. The surface and the bulk change are indicated by electric transport measurements demonstrating compressive strain or positive pressure and tensile strain, analogous to negative pressure, decreasing or increasing the Kondo gap. Initially, our hypothesis was that because pressure and strain have been shown to affect SmB$_6$ through electrical measurements, these factors may be attributed to the inconsistent conclusions from the previous thermal conductivity studies. However, as shown in Figures 4.11 and 4.12, even without strain, the magnitude of our residual term on the order of 10^{-1} mW K^{-2} cm^{-1} is comparable to the study conducted in Cambridge. Through the Wiedemann-Franz Law, electron contribution is on the order of $10^{\wedge -6}$ mW K^{-1} cm^{-1}, meaning that the significant portion of κ linear in T does not originate from electrons. This significant contribution from an unknown source was the reason why the study performed in Cambridge concluded that there might be neutral fermions present in SmB_6, as they have additionally performed their own quantum oscillation measurements suggesting that the oscillations may originate from the bulk [30]. Furthermore, though there was some expected change in the magnitude of the thermal conductivity due to the deformation of the sample, there was an actual considerable change to both the increase in the residual κ as well as the overall behavior in κ in regards to the shift in slope. This measurement implies that differentiating between the different growth methods by themselves is not a dependable predictor. Rather, there seem to be more variable intrinsic properties that are sample dependent, though the general mechanism is unclear. Based on the trend in our strain measurement, uniaxial tensile strain did cause an increase in κ as seen by the change in the phonon contribution affecting the slope of the κ/T. Additional contribution other than from the changing lattice constant may also be due to changes in impurity scattering. Because of this, the application of pressure or compressive strain may show a reversed behavior, with even the possibility of removing the residual term with enough compressive strain. If this was the case, then the intrinsic mechanical perturbations, which seem to be variable even within the same growth methods, could allow this residual term to be tunable.

So far, the observation of quantum oscillations and the residual linear thermal conductivity term is generally credited to charge-neutral fermions, such as from the theorized exciton [45], fractionalized f-hole (the f-electron equivalent of a particle-hole transformation) [46], and the Majorana fermion [30]. However, another possible source could be due to the dislocations, or the one-dimensional defects, that were observed in the 2021 study measuring the bulk resistivity [53]. The study included measuring the density of these dislocations for both flux- and floating-zone grown SmB_6 and noted that floating-zone grown samples contained a higher dislocation density. Their observed bulk resistivity measurements were significant for floating-zone grown samples compared to the flux-grown samples, even with added samarium deficiencies in the flux-grown samples. Because of this observation, dislocations were suggested to be the cause of this sample-dependent low-temperature bulk resistivity in floating-zone grown samples. The observation of the residual linear term in our thermal conductivity measurement could be due to having a higher density of these dislocations in our flux-grown SmB_6, which could be verified by undergoing the same chemical etching procedure. More sample size for acquiring the dislocation density would allow a better reference to this dislocation density threshold that is distinguished between floating-zone and flux-grown SmB6, especially since the floating-zone SmB_6 have a more varying lattice parameter (and thus a more varying dislocation density). If our sample does indeed contain a higher dislocation density, there is a possibility that our sample could also have a low-temperature bulk channel, which would allow the bulk to carry heat.

Our result alone cannot absolutely conclude that there are charge-neutral fermions but only offer a piece of the story for the possible existence of charge-neutral fermions, as our results have added another variation to the other thermal conductivity measurements of flux-grown SmB_6. However, additional experiments can be conducted to add a more compelling image to this result. The first such experiment would be to apply a magnetic field and see if there's a relation between straining and an applied field to the residual term. We were not able to perform this kind of measurement due to our broken helium level probe, where operating a superconducting magnet without a level probe would be dangerous. So far, in regards to the other thermal conductivity studies on flux-grown SmB_6, the application of field does not have a consistent conclusion, where the residual linear term was found to be either insensitive to field [28] or be enhanced by field [29]. It would be interesting to investigate if there's a differing effect on the residual linear term when a field is applied with the same tensile strain. Another experiment that could be conducted would be to use a floating-zone grown SmB_6, as this is where the main contradiction lies for the residual linear term between the study conducted in Sherbrooke [29] and Cambridge [30]. The experimental setup could be used to observe how strain could affect floating-zone grown samples differently compared to the tilted behavioral change of the residual linear term seen on flux-grown SmB_6. Differing reactionary behavior of the thermal conductivity under strain would be another indicator on the significance of different growth methods.

To observe if there is a more direct correlation of the applied strain simulating deficiencies found in floating-zone samples would involve cross-referencing with measurements that use other probing methods. This is due to the deviation from our original observation of the previous studies that the residual linear term of the thermal conductivity was a characteristic present only in floating-zone grown SmB_6. Our measurement shows that the existence of a residual term cannot be reliably used as one of the indicators of simulating deficiencies in floating-zone samples. Instead, multiple thermal conductivity measurements can be done on flux- and floating-zone grown SmB_6 with samarium-deficient flux-grown SmB_6 to observe if there are similarities in behavioral changes of the thermal conductivity with strain. Additionally, electrical measurements such as applying strain to doped flux-grown SmB_6 can be conducted to observe if there is a resistivity decrease as observed in those of doped floating-zone grown SmB_6 but not in doped flux-grown samples [59, 60].

There may be limitations on the availability of conducting certain measurements due to the design and size of the strain apparatus, such as the inverted resistance method using a circular Corbino disk geometry. Being able to measure perform an inverse resistance measurement on strained flux-grown SmB_6 could be done to see if there is a deviation from the perfectly insulating bulk of the flux-grown SmB_6 to bulk conduction of floating-zone grown SmB_6. However, the circular design would make it unavailable to be implemented to the our strain apparatus, as it can apply strain in one dimension.

Bibliography

[1] W. A. Phelan, S. M. Koohpayeh, P. Cottingham, J. A. Tutmaher, J. C. Leiner, M. D. Lumsden, C. M. Lavelle, X. P. Wang, C. Hoffmann, M. A. Siegler, N. Haldolaarachchige, D. P. Young, and T. M. McQueen, *On the Chemistry and Physical Properties of Flux and Floating Zone Grown SmB6 Single Crystals*, Sci Rep **6**, 20860 (2016).

[2] M. Dzero, J. Xia, V. Galitski, and P. Coleman, *Topological Kondo Insulators*, Annual Review of Condensed Matter Physics **7**, 249 (2016).

[3] A. Menth, E. Buehler, and T. H. Geballe, *Magnetic and Semiconducting Properties of Sm B 6*, Phys. Rev. Lett. **22**, 295 (1969).

[4] R. L. Cohen, M. Eibschütz, and K. W. West, *Electronic and Magnetic Structure of Sm B 6*, Phys. Rev. Lett. **24**, 383 (1970).

[5] M. B. Maple and D. Wohlleben, *Nonmagnetic 4 f Shell in the High-Pressure Phase of SmS*, Phys. Rev. Lett. **27**, 511 (1971).

[6] C. M. Varma, *Mixed-Valence Compounds*, Rev. Mod. Phys. **48**, 219 (1976).

[7] Hirst, L.L., *Configuration-Based Ionic Energy Levels and Narrow Energy Bands*, in *Valence Instabilities and Related Narrow-Band Phenomena* (Springer US, 1977), pp. 3--16.

[8] N. F. Mott, *Rare-Earth Compounds with Mixed Valencies*, Philosophical Magazine **30**, 403 (1974).

[9] S. Doniach, *The Kondo Lattice and Weak Antiferromagnetism | EndNote Click*, https://click.endnote.com/viewer?doi=10.1016%2F0378-4363%2877%2990190-5&token=WzIwMDM2MjYsIjEwLjEwMTYvMDM3OC00MzYzKDc3KTkwMTkwLTUiXQ.E9rskaRrF6JDt4hmnffuSkugizs.

[10] C. Lacroix and M. Cyrot, *Phase Diagram of the Kondo Lattice*, Phys. Rev. B **20**, 1969 (1979).

[11] R. Jullien, P. Pfeuty, J. Fields, and S. Doniach, *Theoretical Study of the Kondo Lattice*, Journal de Physique Colloques **40**, C5 (1979).

[12] J. Kondo, *Resistance Minimum in Dilute Magnetic Alloys*, Progress of Theoretical Physics **32**, 37 (1964).

[13] J. W. Allen, B. Batlogg, and P. Wachter, *Large Low-Temperature Hall Effect and Resistivity in Mixed-Valent Sm B 6*, Phys. Rev. B **20**, 4807 (1979).

[14] T. Kasuya, K. Takegahara, T. Fujita, T. Tanaka, and E. Bannai, *Valence Fluctuating State in SmB6*, J. Phys. Colloques **40**, C5 (1979).

[15] J. Jiang, S. Li, T. Zhang, Z. Sun, F. Chen, Z. R. Ye, M. Xu, Q. Q. Ge, S. Y. Tan, X. H. Niu, M. Xia, B. P. Xie, Y. F. Li, X. H. Chen, H. H. Wen, and D. L. Feng, *Observation of Possible Topological In-Gap Surface States in the Kondo Insulator SmB6 by Photoemission*, Nat Commun **4**, 3010 (2013).

[16] M. Neupane, N. Alidoust, S.-Y. Xu, T. Kondo, Y. Ishida, D. J. Kim, C. Liu, I. Belopolski, Y. J. Jo, T.-R. Chang, H.-T. Jeng, T. Durakiewicz, L. Balicas, H. Lin, A. Bansil, S. Shin, Z. Fisk, and M. Z. Hasan, *Surface Electronic Structure of the Topological Kondo-Insulator Candidate Correlated Electron System SmB6*, Nat Commun **4**, 2991 (2013).

[17] N. Xu, P. K. Biswas, J. H. Dil, R. S. Dhaka, G. Landolt, S. Muff, C. E. Matt, X. Shi, N. C. Plumb, M. Radović, E. Pomjakushina, K. Conder, A. Amato, S. V. Borisenko, R. Yu, H.-M. Weng, Z. Fang, X. Dai, J. Mesot, H. Ding, and M. Shi, *Direct Observation of the Spin Texture in SmB6 as Evidence of the Topological Kondo Insulator*, Nat Commun **5**, 4566 (2014).

[18] D. J. Kim, S. Thomas, T. Grant, J. Botimer, Z. Fisk, and J. Xia, *Surface Hall Effect and Nonlocal Transport in SmB6: Evidence for Surface Conduction*, Scientific Reports **3**, (2013).

[19] D. J. Kim, J. Xia, and Z. Fisk, *Topological Surface State in the Kondo Insulator Samarium Hexaboride*, Nature Mater **13**, 466 (2014).

[20] J. Kim, C. Jang, X. Wang, J. Paglione, S. Hong, J. Lee, H. Choi, and D. Kim, *Electrical Detection of the Surface Spin Polarization of the Candidate Topological Kondo Insulator Sm B 6*, Phys. Rev. B **99**, 245148 (2019).

[21] H. Pirie, Y. Liu, A. Soumyanarayanan, P. Chen, Y. He, M. M. Yee, P. F. S. Rosa, J. D. Thompson, D.-J. Kim, Z. Fisk, X. Wang, J. Paglione, D. K. Morr, M. H. Hamidian, and J. E. Hoffman, *Imaging Emergent Heavy Dirac Fermions of a Topological Kondo Insulator*, Nat. Phys. **16**, 52 (2020).

[22] T. Liu, Y. Li, L. Gu, J. Ding, H. Chang, P. A. P. Janantha, B. Kalinikos, V. Novosad, A. Hoffmann, R. Wu, C. L. Chien, and M. Wu, *Nontrivial Nature and Penetration Depth of Topological Surface States in SmB 6 Thin Films*, Phys. Rev. Lett. **120**, 207206 (2018).

[23] L. Jiao, S. Rößler, D. Kasinathan, P. F. S. Rosa, C. Guo, H. Yuan, C.-X. Liu, Z. Fisk, F. Steglich, and S. Wirth, *Magnetic and Defect Probes of the SmB6 Surface State*, Sci Adv **4**, eaau4886 (2018).

[24] G. Li, Z. Xiang, F. Yu, T. Asaba, B. Lawson, P. Cai, C. Tinsman, A. Berkley, S. Wolgast, Y. S. Eo, D.-J. Kim, C. Kurdak, J. W. Allen, K. Sun, X. H. Chen, Y. Y. Wang, Z. Fisk, and L. Li, *Two-Dimensional Fermi Surfaces in Kondo Insulator SmB6*, Science **346**, 1208 (2014).

[25] B. S. Tan, Y.-T. Hsu, B. Zeng, M. C. Hatnean, N. Harrison, Z. Zhu, M. Hartstein, M. Kiourlappou, A. Srivastava, M. D. Johannes, T. P. Murphy, J.-H. Park, L. Balicas, G. G. Lonzarich, G. Balakrishnan, and S. E. Sebastian, *Unconventional Fermi Surface in an Insulating State*, Science **349**, 287 (2015).

[26] Z. Fisk, J. L. Sarrao, J. D. Thompson, D. Mandrus, M. F. Hundley, A. Miglori, B. Bucher, Z. Schlesinger, G. Aeppli, E. Bucher, J. F. DiTusa, C. S. Oglesby, H.-R. Ott, P. C. Canfield, and S. E. Brown, *Kondo Insulators*, Physica B: Condensed Matter **206–207**, 798 (1995).

[27] E. S. Konovalova, Yu. B. Paderno, T. Lundstrem, L. D. Finkel'shtein, N. N. Efremova, and E. M. Dudnik, *Effect of Vacancies and Foreign Metal Ions on the Valent State of Samarium in SmB6*, Powder Metall Met Ceram **21**, 820 (1982).

[28] Y. Xu, S. Cui, J. K. Dong, D. Zhao, T. Wu, X. H. Chen, K. Sun, H. Yao, and S. Y. Li, *Bulk Fermi Surface of Charge-Neutral Excitations in SmB 6 or Not: A Heat-Transport Study*, Phys. Rev. Lett. **116**, 246403 (2016).

[29] M.-E. Boulanger, F. Laliberté, M. Dion, S. Badoux, N. Doiron-Leyraud, W. A. Phelan, S. M. Koohpayeh, W. T. Fuhrman, J. R. Chamorro, T. M. McQueen, X. F. Wang, Y. Nakajima, T. Metz, J. Paglione, and L. Taillefer, *Field-Dependent Heat Transport in the Kondo Insulator SmB 6 : Phonons Scattered by Magnetic Impurities*, Phys. Rev. B **97**, 245141 (2018).

[30] M. Hartstein, W. H. Toews, Y.-T. Hsu, B. Zeng, X. Chen, M. C. Hatnean, Q. R. Zhang, S. Nakamura, A. S. Padgett, G. Rodway-Gant, J. Berk, M. K. Kingston, G. H. Zhang, M. K. Chan, S. Yamashita, T. Sakakibara, Y. Takano, J.-H. Park, L. Balicas, N. Harrison, N. Shitsevalova, G. Balakrishnan, G. G. Lonzarich, R. W. Hill, M. Sutherland, and S. E.

Sebastian, *Fermi Surface in the Absence of a Fermi Liquid in the Kondo Insulator SmB6*, Nat. Phys. **14**, 166 (2018).

[31] M. E. Valentine, S. Koohpayeh, W. A. Phelan, T. M. McQueen, P. F. S. Rosa, Z. Fisk, and N. Drichko, *Breakdown of the Kondo Insulating State in SmB 6 by Introducing Sm Vacancies*, Phys. Rev. B **94**, 075102 (2016).

[32] P. J. Robinson, J. Munarriz, M. E. Valentine, A. Granmoe, N. Drichko, J. R. Chamorro, P. F. Rosa, T. M. McQueen, and A. N. Alexandrova, *Dynamical Bonding Driving Mixed Valency in a Metal Boride*, Angewandte Chemie International Edition **59**, 10996 (2020).

[33] A. Stern, M. Dzero, V. M. Galitski, Z. Fisk, and J. Xia, *Surface-Dominated Conduction up to 240 K in the Kondo Insulator SmB6 under Strain*, Nature Mater **16**, 708 (2017).

[34] S. Wolgast, Ç. Kurdak, K. Sun, J. W. Allen, D.-J. Kim, and Z. Fisk, *Low-Temperature Surface Conduction in the Kondo Insulator SmB 6*, Phys. Rev. B **88**, 180405 (2013).

[35] S. M. Thomas, X. Ding, F. Ronning, V. Zapf, J. D. Thompson, Z. Fisk, J. Xia, and P. F. S. Rosa, *Quantum Oscillations in Flux-Grown SmB 6 with Embedded Aluminum*, Phys. Rev. Lett. **122**, 166401 (2019).

[36] Y. S. Eo, A. Rakoski, J. Lucien, D. Mihaliov, Ç. Kurdak, P. F. S. Rosa, and Z. Fisk, *Transport Gap in SmB $_6$ Protected against Disorder*, Proc Natl Acad Sci USA **116**, 12638 (2019).

[37] Pobell, Frank, *Matter and Methods at Low Temperatures* (Springer, Berlin, Heidelberg, n.d.).

[38] C. Kittel, *Introduction to Solid State Physics*, 8th ed. (John Wiley & Sons, n.d.).

[39] K. Boer and P. Udo, *Semiconductor Physics* (Springer International Publishing AG, n.d.).

[40] H. G. Smith, G. Dolling, S. Kunii, M. Kasaya, B. Liu, K. Takegahara, T. Kasuya, and T. Goto, *Experimental Study of Lattice Dynamics in LaB6 and YbB6*, Solid State Communications **53**, 15 (1985).

[41] S. Y. Li, J.-B. Bonnemaison, A. Payeur, P. Fournier, C. H. Wang, X. H. Chen, and L. Taillefer, *Low-Temperature Phonon Thermal Conductivity of Single-Crystalline Nd 2 Cu O 4 : Effects of Sample Size and Surface Roughness*, Phys. Rev. B **77**, 134501 (2008).

[42] K. Flachbart, *Thermal Conductivity of SmB6*, Journal of the Beg-Common Metals **88**, (n.d.).

[43] J. C. Cooley, M. C. Aronson, Z. Fisk, and P. C. Canfield, *Sm B 6 : Kondo Insulator or Exotic Metal?*, Phys. Rev. Lett. **74**, 1629 (1995).

[44] J. Knolle and N. R. Cooper, *Quantum Oscillations without a Fermi Surface and the Anomalous de Haas–van Alphen Effect*, Phys. Rev. Lett. **115**, 146401 (2015).

[45] J. Knolle and N. R. Cooper, *Excitons in Topological Kondo Insulators: Theory of Thermodynamic and Transport Anomalies in SmB6*, Phys. Rev. Lett. **118**, 096604 (2017).

[46] D. Chowdhury, I. Sodemann, and T. Senthil, *Mixed-Valence Insulators with Neutral Fermi Surfaces*, Nat Commun **9**, 1766 (2018).

[47] J. Stankiewicz, M. Evangelisti, P. F. S. Rosa, P. Schlottmann, and Z. Fisk, *Physical Properties of* Sm_xB_6 *Single Crystals*, Phys. Rev. B **99**, 045138 (2019).

[48] Y. Luo, H. Chen, J. Dai, Z. A. Xu, and J. D. Thompson, Phys. Rev. B **91**, 075130 (2015).

[49] N. E. Sluchanko, A. A. Volkov, V. V. Glushkov, B. P. Gorshunov, S. V. Demishev, M. V. Kondrin, A. A. Pronin, N. A. Samarin, Y. Bruynseraede, V. V. Moshchalkov, and S. Kunii, J. Exp. Theor. Phys. **88**, 533 (1999).

[50] K. Flachbart, S. Gabáni, E. Konovalova, Y. Paderno, and V. Pavlik, Phys. B (Amsterdam, Neth.) **293**, 417 (2001).

[51] S. Gabáni, G. Pristás, I. Takaácˇ ová, N. Sluchanko, K. Siemensmeyer, N. Shitsevalova, V. Filipov, and K. Flachbart, Solid State Sci. **47**, 17 (2015).

[52] P. Hlawenka, K. Siemensmeyer, E. Weschke, A. Varykhalov, J. Sánchez-Barriga, N. Y. Shitsevalova, A. V. Dukhnenko, V. B. Filipov, S. Gabáni, K. Flachbart, O. Rader, and E. D. L. Rienks, Nat. Commun. **9**, 517 (2018).

[53] Y. S. Eo, A. Rakoski, S. Sinha, D. Mihaliov, W. T. Fuhrman, S. R. Saha, P. F. S. Rosa, Z. Fisk, M. C. Hatnean, G. Balakrishnan, J. R. Chamorro, W. A. Phelan, S. M. Koohpayeh, T. M. McQueen, B. Kang, M. Song, B. Cho, M. S. Fuhrer, J. Paglione, and Ç. Kurdak, *Bulk Transport Paths through Defects in Floating Zone and Al Flux Grown SmB6* Phys. Rev. Materials **5**, 055001 (2021).

[54] K. Chen, T-C. Weng, G. Schmerber, V. N. Gurin, J.-P. Kappler, Q. Kong, F. Baudelet, A. Polian, and L. Nataf. Phys. Rev. B 97, 235153 (2018)

[55] W. T. Fuhrman, J. C. Leiner, J. W. Freeland, M. van Veenendaal, S. M. Koohpayeh, W. Adam Phelan, T. M. McQueen, and C. Broholm. Phys. Rev. B 99, 020401(R) (2019)

[56] W. T. Fuhrman, J. R. Chamorro, P. A. Alekseev, J.-M. Mignot, T. Keller, J. A. Rodriguez-Rivera, Y. Qiu, P. Nikolić, T. M. McQueen & C. L. Broholm. Nature Communications volume 9, Article number: 1539 (2018)

[57] Y. Sato, Z. Xiang, Y. Kasahara, T. Taniguchi, S. Kasahara, L. Chen, T. Asaba, C. Tinsman, H. Murayama, O. Tanaka, Y. Mizukami, T. Shibauchi, F. Iga, J. Singleton, L. Li, and Y. Matsuda, *Unconventional Thermal Metallic State of Charge-Neutral Fermions in an Insulator*, Nat. Phys. **15**, 954 (2019).

[58] Chamorro, W. Adam Phelan, Seyed M. Koohpayeh, Tyrel M. McQueen, Boyoun Kang, Myung-suk Song, Beongki Cho, Michael S. Fuhrer, Johnpierre Paglione, and Çağlıyan Kurdak. Phys. Rev. Materials 5, 055001 (2021)

[59] S. Gabáni, M. Orendácˇ, G. Pristáš, E. Gažo, P. Diko, S. Piovarcˇi, V. Glushkov, N. Sluchanko, A. Levchenko, N. Shitsevalova, and K. Flachbart, Philos. Mag. **96**, 3274 (2016).

[60] G. Pristáš, S. Gabáni, K. Flachbart, V. Filipov, and N. Shitseval- ova, JPS Conf. Proc. **3**, 012021 (2014).

[61] Y. Zhou, P. F. S. Rosa, J. Guo, S. Cai, R. Yu, S. Jiang, K. Yang, A. Li, Q. Si, Q. Wu, Z. Fisk, and L. Sun, *Hall Coefficient Diagnostics of Surface State in Pressurized SmB6*, Phys. Rev. B **101**, 125116 (2020).